

DTIC
S
ELECTE
C
D

2

SC71041.FR

AUG 31 1993

AFOSR-TR- 93 06 40 Copy No. 3

SC71041.FR

**PHOTOREFRACTIVE TUNGSTEN BRONZE CRYSTALS
FOR OPTICAL COMPUTING**

FINAL REPORT FOR THE PERIOD

September 24, 1990 through March 23, 1993

AD-A268 859



CONTRACT NO. F49620-90-C-0089

Prepared for

**Air Force Office of Scientific Research
Bolling AFB
Washington, DC 20332**

**R. R. Neurgaonkar
Principal Investigator**

July 1993

Approved for public release; distribution unlimited.

The views and conclusions contained in this document are those of the authors and should not be interpreted as necessarily representing the official policies, either expressed or implied, of the Defense Advanced Research Projects Agency or the U. S. Government.



**Rockwell International
Science Center**

93-20265



93 8 30 02 8

7800

UNCLASSIFIED

SECURITY CLASSIFICATION OF THIS PAGE

REPORT DOCUMENTATION PAGE				FORM APPROVED OMB No. 0704-0188	
1a. REPORT SECURITY CLASSIFICATION Unclassified			1b. RESTRICTIVE MARKINGS		
2a. SECURITY CLASSIFICATION AUTHORITY			3. DISTRIBUTION/AVAILABILITY OF REPORT Approved for public release; distribution is unlimited.		
2b. CLASSIFICATION/DOWNGRADING SCHEDULE					
4. PERFORMING ORGANIZATION REPORT NUMBER(S) SC 71041			5. MONITORING ORGANIZATION REPORT NUMBER(S)		
6a. NAME OF PERFORMING ORGANIZATION Rockwell International Science Center		6b. OFFICE SYMBOL (If Applicable)	7a. NAME OF MONITORING ORGANIZATION AFOSR/NE		
6c. ADDRESS (City, State and ZIP Code) 1049 Camino Dos Rios Thousand Oaks, CA 91360			7b. ADDRESS (City, State and ZIP Code) 1100 Duncan Ave BAFB DC 20332-0001		
8a. NAME OF FUNDING/SPONSORING ORGANIZATION DARPA		8b. OFFICE SYMBOL (If Applicable)	9. PROCUREMENT INSTRUMENT IDENTIFICATION NUMBER Contract No. F49620-90-C-0089		
8c. ADDRESS (City, State and ZIP Code) 1400 Wilson Blvd Arlington Va 22209			10. SOURCE OF FUNDING NOS.	TASK NO.	WORK UNIT ACCESSION NO.
			PROGRAM ELEMENT NO. 61101E	PROJECT NO. 7321 DARPA	00
11. TITLE (Include Security Classification) PHOTOREFRACTIVE TUNGSTEN BRONZE CRYSTALS FOR OPTICAL COMPUTING					
12. PERSONAL AUTHOR(S) Neurgaonkar, Ratnakar R.					
13a. TYPE OF REPORT Final Report		13b. TIME COVERED FROM 09/24/90 TO 03/23/93		14. DATE OF REPORT (Year, Month, Day) 1993, July 23	
15. PAGE COUNT					
16. SUPPLEMENTARY NOTATION Reproduction in whole or in part is permitted for any purpose of the US Government.					
17. COSATI CODES			18. SUBJECT TERMS (Continue on reverse if necessary and identify by block number)		
FIELD	GROUP	SUB-GROUP	Optical computing, hologram, T.B. crystals, dielectric, electro-optic and photorefractive effects. Crystal growth, data storage, pattern recognition.		
19. ABSTRACT (Continue on reverse if necessary and identify by block number) We have identified and grown new photorefractive tungsten bronze BSTN and BSKNN single crystals for optical computing applications. These crystals exhibit faster response times than the current best SBN:60 with comparable doping concentrations. At Caltech, holographic fixation has been demonstrated in Rh- and Cr-doped SBN:75 single crystals. Because of such features, various applications in the areas of data storage, optical pattern recognition and optical computing are emerging for these tungsten bronze crystals.					
20. DISTRIBUTION/AVAILABILITY OF ABSTRACT Same as report			21. ABSTRACT SECURITY CLASSIFICATION Unclassified		
22a. NAME OF RESPONSIBLE INDIVIDUAL Craig			22b. TELEPHONE NUMBER (INCLUDE AREA CODE) 202-767-4931		22c. OFFICE SYMBOL NE

DD FORM 1473

Previous editions are obsolete.

UNCLASSIFIED

SECURITY CLASSIFICATION OF THIS PAGE



TABLE OF CONTENTS

	Page
1.0 PROGRESS SUMMARY	1
2.0 INTRODUCTION	2
3.0 PROGRESS	4
3.1 Accomplishments at Rockwell	4
3.1.1 Growth of Tungsten Bronze Crystals	4
3.1.2 Role of Dopants	9
3.2 Accomplishments at Caltech	10
3.2.1 Photorefractive Characterization	10
3.2.2 Holographic Disk Development	12
3.2.3 Fixation of Holograms in Tungsten Bronze Crystals	13
4.0 CONCLUSIONS AND RECOMMENDATIONS	15
4.1 Growth of BSTN Crystals	15
4.2 Storage Time vs Dark Conductivity	16
4.3 Holographic Fixation	17
4.4 Fabrication of Memory Disks	18
5.0 REFERENCES	19
 6.0 APPENDIX (PUBLICATIONS)	
6.1 Ferroelectric and optical properties of T. B. $(\text{Ba,Sr})_6\text{Ti}_2\text{Nb}_8\text{O}_{30}$ Single Crystals	20
6.2 Ferroelectric properties of $(\text{Ba,Sr})_6\text{Ti}_2\text{Nb}_8\text{O}_{30}$ single crystals	21
6.3 Electrical fixing of photorefractive holograms in SBN:75	22
6.4 Dynamic electronic compensation of fixed gratings in photorefractive media	23



Rockwell International
Science Center
SC71041.FR

TABLE OF CONTENTS (cont.)

	Page
6.5 Electric-field multiplexing/demultiplexing of volume holograms in photorefractive media	24
6.6 Beam coupling and spatial mode conversion in photorefractive planar waveguides	25

DTIC QUALITY INSPECTED 3

Accession For	
NTIS CRA&I	<input checked="checked" type="checkbox"/>
DTIC TAB	<input type="checkbox"/>
Unannounced	<input type="checkbox"/>
Justification	
By	
Distribution /	
Availability Codes	
Dist	Avail and/or Special
A-1	



LIST OF FIGURES

	<u>Page</u>
2.1 Photorefractive tungsten bronze crystals for optical computing	3
3.1 Chronological development of tungsten bronze ferroelectric crystals	5
3.2 Czochralski-grown Ce-doped BSTN single crystal	7
3.3 Czochralski-grown Ce-doped KBN single crystal	8
3.4 The role of dopants in tungsten bronze crystals	9
3.5 Intensity of the diffracted light as a function of time	10
3.6 Changes in the diffraction efficiency with time	11
3.7 Schematic diagram of a 3-D memory system	12
3.8 Diffraction efficiency η as a function of the disk rotation angle for LiNbO_3	13
3.9 Diffraction efficiency as a function of time for fixing with a negative voltage pulse	14
4.1 Effect of external electric field on photorefractive properties	16
4.2 Dark conductivity in various photorefractive crystals	17

LIST OF TABLES

	<u>Page</u>
2.1 Photorefractive Tungsten Bronze Crystals For Optical Computing	2



1.0 PROGRESS SUMMARY

This report covers the work on photorefractive tungsten bronze crystals for optical computing carried out over the period of September 24, 1991, through March 23, 1993, in the Ferroelectric Materials Department of the Rockwell International Science Center under Contract No. F49620-90-C-0089. During this period, significant progress was made in the growth of tungsten bronze $(\text{Ba,Sr})_6\text{Ti}_2\text{Nb}_8\text{O}_{30}$ (BSTN), $\text{Ba}_{2-x}\text{Sr}_x\text{K}_{1-y}\text{Na}_y\text{Nb}_5\text{O}_{15}$ (BSKNN) and $\text{K}_2\text{BiNb}_5\text{O}_{15}$ (KBN) single crystals and the improvement of their photorefractive properties with respect to optical computing applications. At Caltech, D.Psaltis and his group have characterized and studied the performance of these materials for a number of optical computing device configurations, including 3-D memory storage and pattern recognition.

Because outstanding photorefractive properties and large size crystals are achievable within the tungsten bronzes, this family offers a wide base of materials for optical computing applications. Recent demonstration of the fixation of holograms in these materials is one step forward towards that end. Implementation of various device concepts using these materials for different memory and pattern recognition applications is underway.



2.0 INTRODUCTION

The main objective of this work is to utilize the large photorefractive properties and variable spectral response (0.4 to 1.0 μm) available in high figure-of-merit ($n^3 r_{ij}/\epsilon$) tungsten bronze ($\text{Ba,Sr}_6\text{Ti}_2\text{Nb}_8\text{O}_{30}$ (BSTN), $\text{Sr}_{2-x}\text{Ca}_x\text{NaNb}_5\text{O}_{15}$ (SCNN), $\text{Ba}_{2-x}\text{Sr}_x\text{K}_{1-y}\text{Na}_y\text{Nb}_5\text{O}_{15}$ (BSKNN) and $\text{K}_2\text{BiNb}_5\text{O}_{15}$ (KBN) single crystals to achieve exceptional performance in various short and long term holographic storage, pattern recognition, image processing and interconnect applications. Table 2.1 summarizes the ferroelectric and optical properties of these high figure-of-merit tungsten bronze crystals. The work includes the necessary modifications in crystal compositions, growth techniques and doping schemes to achieve the desired crystals size, quality and spectral range. This is the first time these tungsten bronze crystals are available for optical computing and they have distinct advantages over the current best candidates such as LiNbO_3 , BaTiO_3 and SBN. We expect that these materials will provide the desired storage time and storage capacity needed for various applications.

Table 2.1
Photorefractive Tungsten Bronze Crystals For Optical Computing

Composition	T_c ($^{\circ}\text{C}$)	ϵ	r_{ij} (10^{-12} m/V)	$n^3 r_{ij}/\epsilon$	Crystal dia. (cm)
BSTN (3:2)	170	$\epsilon_{33} = 230$	$r_{33} = 135$	8.3	> 1.5
BSTN (2.5:3.5)	116	$\epsilon_{33} = 345$	$r_{33} = 200$	8.2	~ 2.0
SCNN (2:90:8))	270	$\epsilon_{33} = 1740$	$r_{33} = 1200$	8.1	> 1.0
		$\epsilon_{11} = 1700$	$r_{51} = 1150$	7.9	
BSKNN-5	180	$\epsilon_{33} = 250$	$r_{33} = 125$	6.3	~ 2.0
		$\epsilon_{11} = 1000$	$r_{51} = 400$	7.5	

r_{ij} = electro-optic coefficient and ϵ = dielectric constant



Photorefractive single crystals developed under this program are being evaluated for optical computing applications at Caltech (D. Psaltis), UCSD (Sing Lee) and at Rockwell International (J. Hong) and based on these results, the necessary modifications in photorefractive crystals are being made to achieve the desired material performance. Recently, Psaltis and his group demonstrated the fixing of holograms in tungsten bronze crystals and this will speed up our holographic storage work. They have also planned various configuration to build optical disks for many different applications. The overall goals of this program are summarized in Figure 2.1.

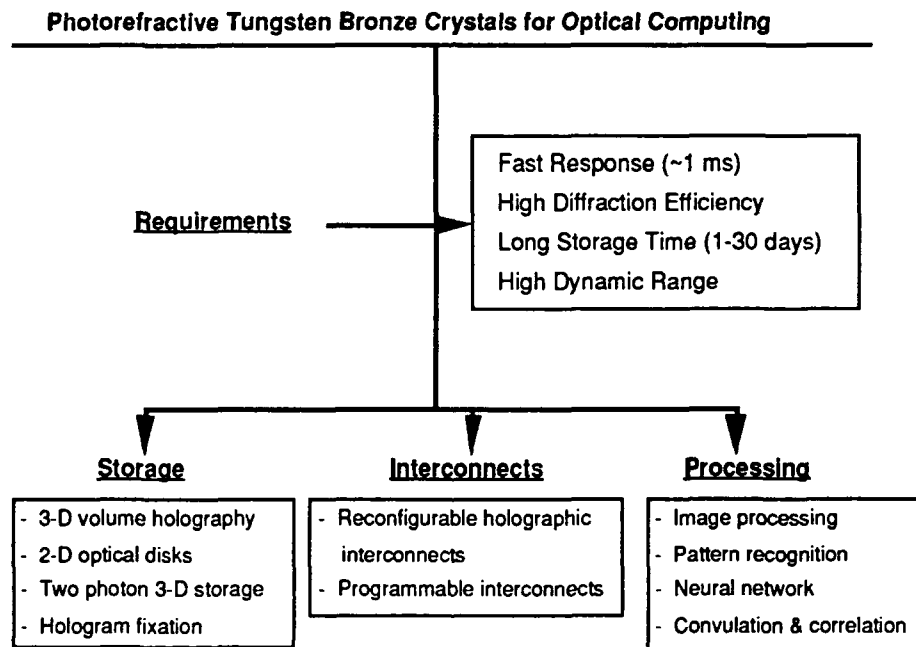


Figure 2.1 -- Photorefractive tungsten bronze crystals for optical computing.



3.0 PROGRESS

During the past 30 months, significant progress was made in the development of high optical figure-of-merit new tungsten bronze (T. B.) ferroelectric materials for optical computing. This includes the growth of good quality doped photorefractive $(\text{Ba,Sr})_6\text{Ti}_2\text{Nb}_8\text{O}_{30}$ (BSTN), $\text{K}_2\text{BiNb}_5\text{O}_{15}$ (KBN), $\text{Ba}_{2-x}\text{Sr}_x\text{K}_{1-y}\text{Na}_y\text{Nb}_5\text{O}_{15}$ (BSKNN) and $\text{Sr}_{2-x}\text{Ca}_x\text{NaNb}_5\text{O}_{15}$ (SCNN) single crystals, and the characterization of their ferroelectric and optical properties at Rockwell International. The photorefractive properties and their applicability to optical computing has been evaluated jointly at Caltech and Rockwell. The summary of our progress is as follows:

3.1 Accomplishments at Rockwell

3.1.1 Growth of Tungsten Bronze Crystals

Under this program, we have successfully grown and characterized tungsten bronze BSTN, SCNN, BSKNN-5 and KBN single crystals for optical computing. This work is a part of our continuing long-range effort to identify and grow high optical figure-of-merit tungsten bronze crystals. Figure 3.1 summarizes the chronological development of tungsten bronze crystals in our laboratory. The new bronzes such as BSTN, SCNN, BSKNN and KBN were identified and grown from this general scheme because they possess approximately two times larger optical figures-of-merit (Table 2.1) than the current best SBN and BaTiO_3 . The BSTN and SCNN solid solution systems have been studied for the first time in our laboratory and they are extremely good candidates for photorefractive applications. KBN is a well known crystal system which has been primarily used as substrate materials.

The electro-optic and ferroelectric properties of tungsten bronze BSTN, SCNN and BSKNN crystals are distinctly different from one another:

- | | |
|----------|--|
| 1. BSTN: | - Large transverse electro-optic coefficient, r_{33}
- Filled tungsten bronze structure with 4 mm symmetry
- Almost no relaxor character |
| 2. BSKNN | - Large longitudinal electro-optic coefficient, r_{51} |



- Filled tungsten bronze structure with 4 mm symmetry
- Almost no relaxor character

3. SCNN and KBN:

- Large r_{33} and r_{51} coefficients
- Filled tungsten bronze structure with mm2 symmetry
- Low relaxor character

It is interesting to note that BSTN crystals behave like SBN in their electro-optic and photorefractive characters, while BSKNN crystals resembles to BaTiO_3 . SCNN crystals combine all of these features; hence this crystal is potentially important for data storage and holographic memory applications. However, SCNN crystals are more difficult to grow because they are orthorhombic at room temperature and undergo two phase transitions during cooldown from elevated temperatures.

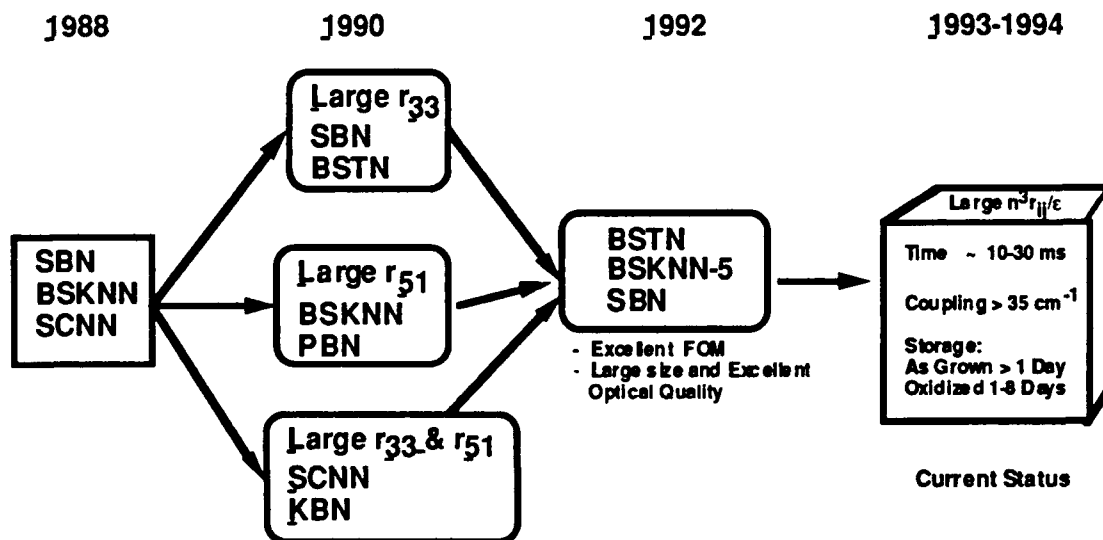


Figure 3.1 -- Chronological development of tungsten bronze ferroelectric crystals.



All of these new crystals have been grown by the Czochralski technique equipped with an automatic diameter controlled (ADC) unit and we have been successful in growing a number of BSTN, BSKNN, SCNN and KBN crystals doped with Ce and Rh in optical quality. A brief summary of our work is given below:

<u>Crystal Composition</u>	<u>Growth Temp (°C)</u>	<u>Crystal Diameter (cm)</u>
BSTN (2:1)	1490	~ 1.8
BSTN (2.5:3.5)	1495	> 1.8
BSKNN-5	1470	~ 1.0
SCNN (9:1)	1505	~ 1.0
KBN	1050	> 2.0

BSTN Crystals: Crystals grown in this study are tetragonal at room temperature and show almost no relaxor character. Ferroelectric and optical characterization of BSTN indicates that the optical figure-of-merit ($n^3 r_{ij} / \epsilon$) is almost two times larger than for photorefractive SBN:60 and BaTiO₃ crystals with significantly higher phase transition temperatures. The speed, coupling and storage time are better than in SBN due to a low dielectric constant and are significantly enhanced with the application of an electric field. Currently, these crystals are being grown in excess of 1.8 cm diameter as shown in Figure 3.2, and we expect that the size can be increased to 4 cm by adjusting the growth conditions. Detailed information on the phase diagram, growth conditions, and ferroelectric and photorefractive properties are given in the attached papers (Appendix 6.1 and 6.2).

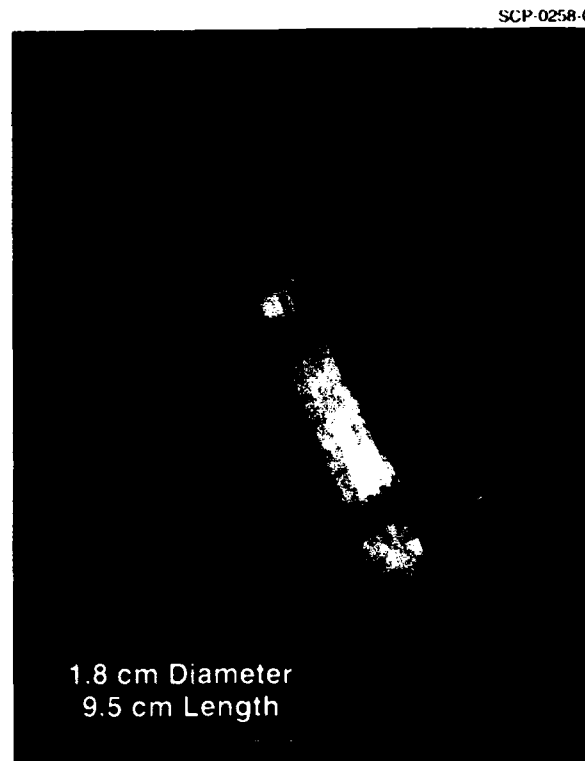


Figure 3.2 -- Czochralski-grown Ce-doped BSTN single crystal.

BSKNN-5 Crystals: This crystal is tetragonal at room temperature and it resembles BaTiO_3 in its electro-optic character. The speed and coupling are slightly better than BaTiO_3 and they also exhibit enhanced performance with the application of external field ($\sim 5 \text{ kV/cm}$). These crystals are easier to grow than BSTN and currently we have grown these crystals in sizes up to 2.5 cm diameter with excellent optical quality.

SCNN Crystals: Orthorhombic tungsten bronze SCNN crystals indicate large and nearly equal transverse (r_{33}) and longitudinal (r_{51}) electro-optic effects, thus combining the excellent features of both SBN and BaTiO_3 . These crystals could therefore have a significant impact on 3-dimensional storage applications. This composition also exhibits a high T_c (270°C) and it has a filled bronze structure and consequently should show higher storage times. However, since SCNN has two phase transitions above room



temperature, larger crystals crack on cooling through these phase transitions. Our recent work on SCNN indicates that the addition of Ba^{2+} reduces the cracking of crystals while maintaining reasonably high electro-optic coefficients. We plan to continue BSCNN growth in this program with other suitable cations for optical computing studies. If we succeed in scaling up crystal size for this crystal, it could have great potential for various optical functions.

KBN Crystals: These crystals are orthorhombic (mm^2) at room temperature and, as shown in Figure 3.3, can be grown in large sizes. These Bi^{3+} -containing crystals exhibit a spectral response beyond $1.0 \mu\text{m}$ and could be potentially useful in that spectral range. At present there is no oxide single crystal which is good in this region. However, we have been unsuccessful in identifying the true polar direction in these crystals. Currently, efforts are underway to determine the polar direction and then we will establish its importance for optical computing.



Figure 3.3 -- Czochralski grown Ce-doped KBN single crystal.



3.1.2 · Role of Dopants

Dopants provide the traps that are essential for photorefractive response in tungsten bronze crystals. During the course of this study, we optimized the use of various dopants in pairs (double doping) chosen to achieve the desired speed, coupling and dark conductivity necessary for optical computing functions. Figure 3.4 summarizes the criteria we used to select these dopants in our work.

We have systematically investigated the role of various dopants in BSTN and BSKNN-5 and found that combinations such as $\text{Ce}^{3+} + \text{Fe}^{3+}$ and $\text{Ce}^{3+} + \text{Mn}^{3+}$ are suitable to achieve the desired speed, coupling and dark conductivity. Further efforts are under way to enhance these properties, specifically the storage time, by optimizing the concentration of these dopants and their site preferences in these crystals. Our current best results are:

- Speed of Response: 20-60 ms
- Coupling: $> 20 \text{ cm}^{-1}$
- Dark Conductivity: 10^{-15} to $10^{-16} \text{ ohm}^{-1}\text{-cm}^{-1}$

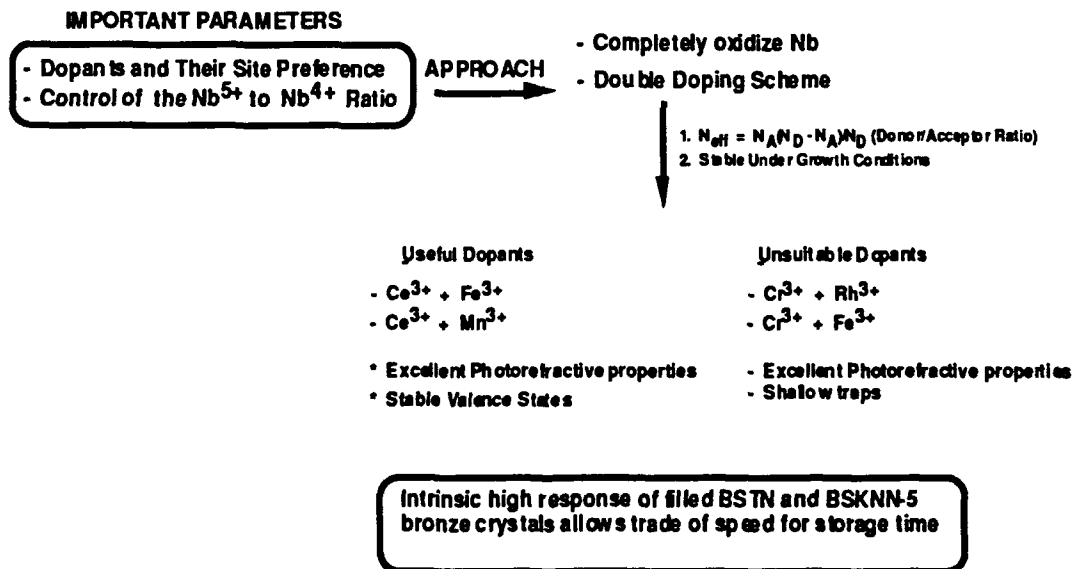


Figure 3.4 -- The role of dopants in tungsten bronze crystals.



3.2 Accomplishments at Caltech

3.2.1 Photorefractive Characterization

1. Ce-doped BSTN has been experimentally characterized in terms of photorefractive sensitivity and two-wave coupling gain. Figure 3.5 shows typical experimental data for the intensity of diffracted light as a function of time. The sensitivity derived from this measurement for BSTN is about 64 mJ/cm^2 . This sensitivity is much better than that of the best Ce-doped SBN:60 and BaTiO_3 photorefractive crystals. We expect that these properties will be substantially enhanced by adjusting the proper doping concentrations and improving the crystal quality. The improvements in photorefractive properties for BSTN are related to the higher optical figure-of-merit in this material.

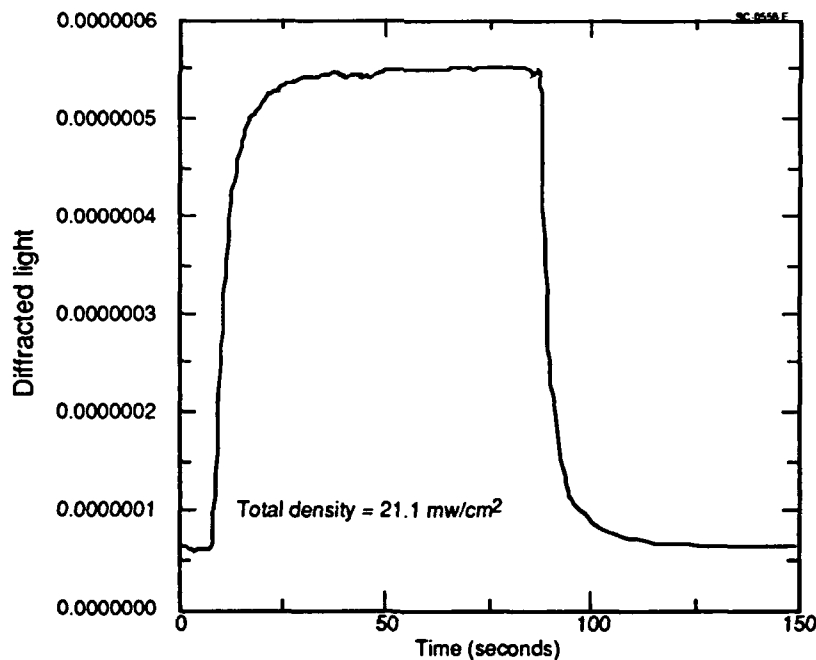


Figure 3.5 -- Intensity of the diffracted light as a function of time.



2. A two-wave coupling gain of 25 cm^{-1} was measured for the same BSTN crystal. Preliminary measurements under an applied field of 5 kV/cm show a significant increase in coupling ($> 30 \text{ cm}^{-1}$). Similar measurements on SBN:60 and BSKNN-2 under applied field have shown that both the diffraction efficiency and the ratio of erasing time to writing time increase dramatically.¹ The sensitivity of gain with applied field in Ce-doped BSTN indicates that these key properties will also increase significantly in BSTN.
3. A method for maintaining recorded holograms during read-out has been demonstrated using a tungsten bronze SBN crystal for storage and two BaTiO_3 crystals as phase conjugate mirrors. Figure 3.6 shows experimental curves for the change in hologram diffraction efficiency with time. Under these three conditions the system reached an overall steady state diffraction efficiency of about 0.845%, independent of the initial conditions. By this means the strong photorefractive properties available in tungsten bronze materials can be used for non-volatile storage with better performance.

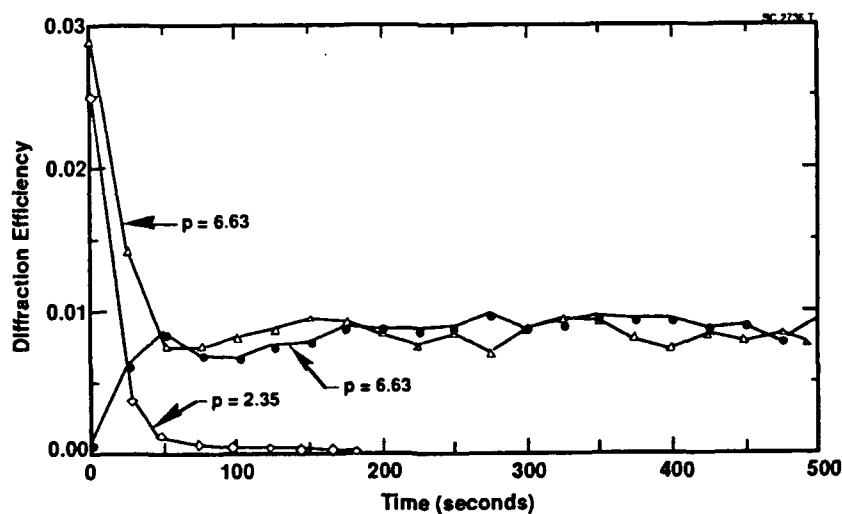


Figure 3.6 -- Changes in the diffraction efficiency with time.



applications. Also, we anticipate that the dark conductivity should be low in these crystals and thus they should retain holograms for longer periods than SBN and BaTiO₃.

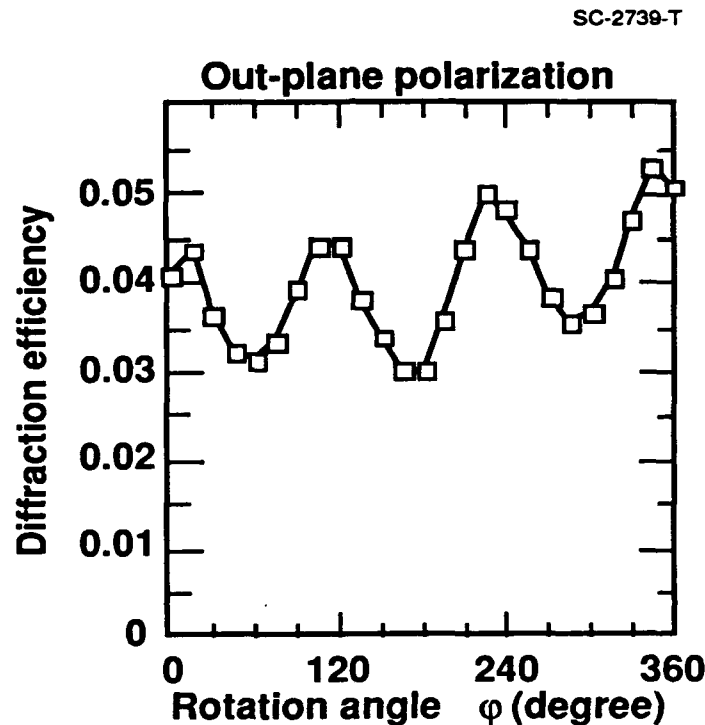


Figure 3.8 -- Diffraction efficiency η as a function of the disk rotation angle for LiNbO₃.

3.2.3 Fixation of Holograms in Tungsten Bronze Crystals

Photorefractive holograms stored in Sr_{0.75}Ba_{0.25}Nb₂O₆ (SBN:75) crystals have been electrically fixed at room temperature. This is the first time holographic fixation has been achieved in this family of materials and this will allow us to fabricate various disks for 3-D and 2-D memories as well as for optical pattern recognition. The fixed holograms can be read out directly or after the application of a positive voltage which can dramatically enhance the diffraction efficiency. Single gratings as well as images can be recorded and fixed.



3.2.2 Holographic Disk Development

A number of concepts for implementing 3-D memory storage using tungsten bronze crystals have been identified (Figure 3.7), and their storage capacities have been estimated. With a 5 cm diameter disk, and each hologram occupying 10 mm^2 of the disk and 1,000 holograms superimposed at each location, the total storage capacity approaches 2×10^{11} pixels.

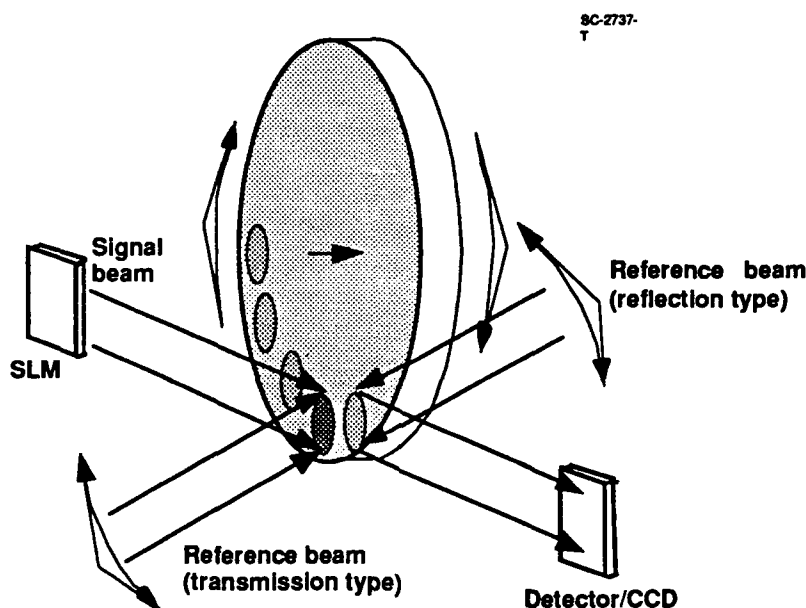


Figure 3.7 -- Schematic diagram of 3-D memory system.

Figure 3.8 shows the experimental curve of diffraction efficiency as a function of the disk rotation angle for LiNbO_3 . Note that there is a 3-fold symmetry along the rotational axis. For crystals belonging to the 4mm symmetry such as BSTN, SBN or BaTiO_3 , the diffraction efficiency should be independent of the rotational angle.

Both BSTN and BSCNN offer significant advantages over LiNbO_3 , SBN:60 and BaTiO_3 because of their superior photorefractive properties. In both of these crystals, holograms can be written much faster, while in BSCNN the storage capacity is greater because two large electro-optic coefficients are available for writing holograms. This is a unique crystal for holographic



The crystal sample used in the experiment was grown and poled at the Rockwell International Science Center. This sample was Rh^{3+} -doped with dimensions of 6 x 6 x 6 mm, with its c axis parallel to the edge. An external electric field was applied along the c axis, and it is called positive as its direction is same as that of the initial poling field. In this experiment, a holographic grating was recorded in the completely poled crystal without any applied field. After the diffraction efficiency reached its saturation value, the recording beams were blocked and a negative voltage pulse with amplitude $V = -1 \text{ kV}$ and duration $t = 0.5 \text{ sec.}$ was applied to the crystal, which caused diffraction efficiency to fall quickly. After the voltage pulse was removed, diffraction efficiency recovered to a portion of its initial value before the pulse. Then the crystal was illuminated with a non-Bragg-matched erasing beam, and diffraction efficiency decreased further until it reached a steady state value of $\sim 0.06\%$. This fixed grating could not be erased by the erasing beam. Then the erasing beam was blocked and a positive voltage pulse, with amplitude $= +2 \text{ kV}$ and duration of a few seconds, was applied to the crystal. During the positive voltage pulse the diffraction efficiency was 1.8% and after the pulse a grating with diffraction efficiency of 0.4% was revealed. This revealed grating can be optically erased. The experimental results of recording, fixing, revealing, and erasure are shown in Figure 3.9.

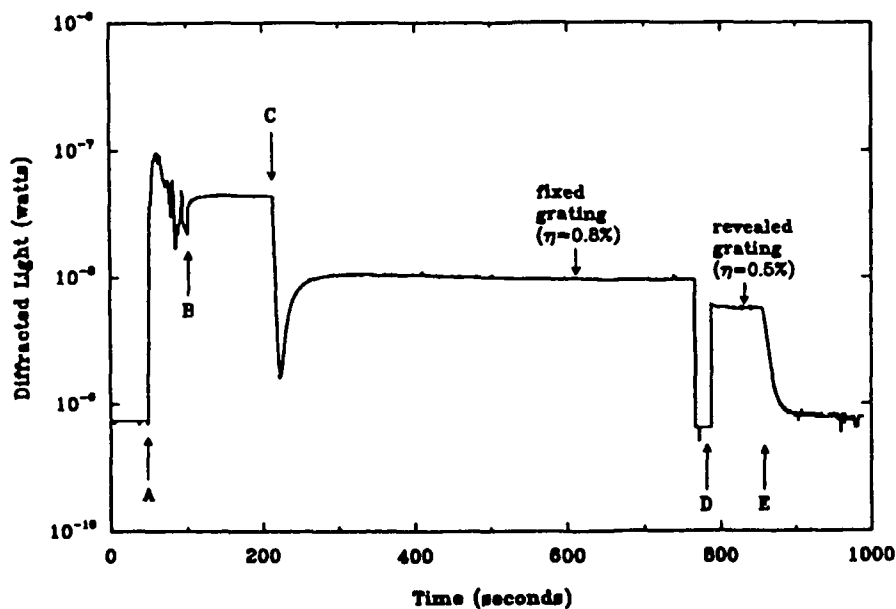


Figure 3.9 -- Diffraction efficiency as a function of time for fixing with a negative voltage pulse.



4.0 CONCLUSIONS AND RECOMMENDATIONS

We propose the following recommendation for future research work in this area:

1. Improve crystal quality of BSTN and BSKNN-5
2. Storage time vs dark conductivity.
3. Holographic fixation and memory device concepts.

4.1 Growth of BSTN and BSKNN Crystals

We will continue to improve the crystal quality and size of these crystals. In the case of BSTN, we have begun to control the thermal gradient in the melt via computer control, and we expect that higher optical quality will be achieved, as we have previously demonstrated for related tungsten bronze crystals.¹⁻⁵ Once we achieve sufficient optical quality, we will scale up the size of this crystal from 1.8 cm to 4.0 cm diameter. Since BSTN compositions are tetragonal at room temperature, cracking of large crystals during cool-down through the ferroelectric phase transition is generally not a problem.

BSTN crystals are being doped with cerium ($\text{Ce}^{3+}/\text{Ce}^{+}$) and Rh^{3+} , and once their role is established, we will try other dopants in these crystals. Photorefractive measurements show that the coupling for Ce-doped BSTN is significantly higher than Ce-doped SBN:60 with longer storage times.

The application of an external electric field has a pronounced effect on all photorefractive properties, and as discussed earlier, it also makes it possible to fix holograms in these crystals. Figure 4.1 summarizes our work tungsten bronze SBN and BSTN crystals using an external field. We found that the application of such a field enhances the speed of response by an order of magnitude and the diffraction efficiency by the factor 25 for SBN and 24 for BSTN, respectively. We will continue to explore the effects of external fields on the photorefractive properties and the fixation of holograms in these tungsten bronze crystals.

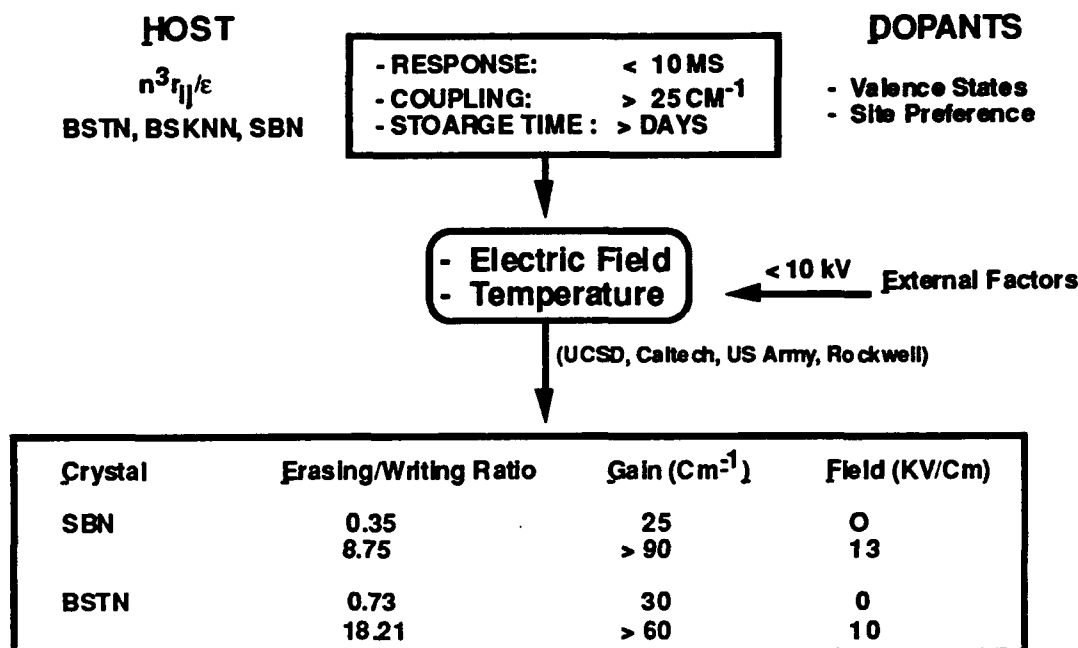
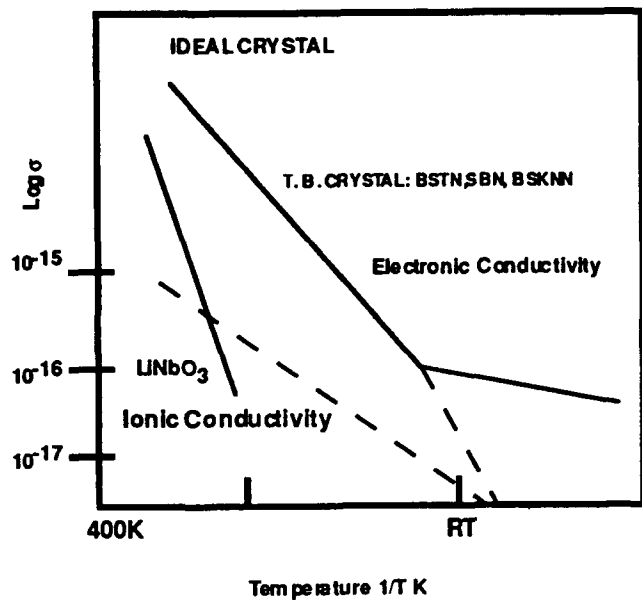


Figure 4.1 -- Effect of external electric field on photorefractive properties.

4.2 Storage Time vs Dark Conductivity

The dark conductivity in tungsten bronze crystals is controlled by structural defects (15- and 12-fold sites partially empty), impurities and the valence states of both host and dopant cations (Fig. 4.2). Structural defects can be reduced by utilizing filled bronze phases, e.g. BSTN, BSCNN or BSKNN-5, while valence states are sensitive to oxidation-reduction conditions present during growth. To achieve controllable and uniform oxidation/reduction in a given sample, we need to address the following factors:

1. Diffusion (O₂ vacancy) : Sample thickness, temperature and time
2. Control of Nb⁵⁺ : Temperature and O₂ partial pressure



Problem: Conductivity $< 10^{-17}$

- Defects and Vacancies
- Site Preferences of Donor/Acceptor
- Location of Fermi Level

Problem: Conductivity $< 10^{-15}$

- Impurity Levels in Starting Materials
- Donor:Acceptor Ratio

Crystal Conductivity ($\Omega^{-1}\text{cm}^{-1}$)

LINbO ₃	10^{-17} to 10^{-18}
SBN:60	10^{-15} to 10^{-16}
BSTN	$< 10^{-16}$

Figure 4.2-- Dark conductivity in various photorefractive crystals.

We will study in detail the valence states of each dopant and their effects on dark conductivity under partially reducing and oxidizing conditions. Based on this study, optimal processing conditions for the selected dopants will be determined.

4.3 Holographic Fixation

We will continue to investigate holographic fixing in tungsten bronze SBN:75 and BSTN crystals. We know from our current experiments that an external electric field is essential, but details of the actual fixation process and its optimization are not well understood. At Caltech, Professor Psaltis and his group are establishing the factors that are responsible for this phenomenon.



4.4 Fabrication of Memory Disks

The ability to fix holograms in tungsten bronze crystals opens up the potential for holographic memory disks and optical pattern recognition. At Caltech, Professor Psaltis and his group are presently adapting the technology established for LiNbO_3 to tungsten bronze materials, with the expectation that the bronzes will be more effective in their performance.



5.0 **REFERENCES**

1. R. R. Neurgaonkar, W. W. Ho, W. K. Cory, W. F. Hall and L. E. Cross, *Ferroelectrics* 51, 185 (1984).
2. R. R. Neurgaonkar and W. K. Cory, *J. Opt. Soc. Am.* 3(B), 276 (1986).
3. R. R. Neurgaonkar, W. K. Cory, J. R. Oliver, M. D. Ewbank and H. F. Hall, *J. Opt. Engineering* 26(5), 392 (1987).
4. R. R. Neurgaonkar, W. K. Cory, J. R. Oliver, M. J. Miller, W. W. Clark III, G. L. Wood and E. J. Sharp, *J. Cryst. Growth* 84, 629 (1987).
5. R. R. Neurgaonkar, W. K. Cory, J. R. Oliver and L. E. Cross, *Mat. Res. Bull.* 24, 1025 (1989).



Rockwell International
Science Center
SC71041.FR

APPENDIX 6.1

FERROELECTRIC AND OPTICAL PROPERTIES OF TUNGSTEN BRONZE (Ba, Sr)₆Ti₂Nb₈O₃₀ SINGLE CRYSTALS

FERROELECTRIC AND OPTICAL PROPERTIES OF TUNGSTEN BRONZE (Ba,Sr)₆Ti₂Nb₈O₃₀ SINGLE CRYSTALS

R.R.Neurgaonkar, W. K. Cory and J. R. Oliver
Rockwell International Science Center
Thousand oaks, CA 91360

and

E. J. Sharp, G. L. Wood
Army Research Laboratory
Fort Belvoir, VA 22060-5028

and

G. J. Salamo
University of Arkansas
Fayetteville, AR 72701

ABSTRACT

Ferroelectric tungsten bronze single crystals based on the (Ba,Sr)₆Ti₂Nb₈O₃₀ system have been grown by the Czochralski technique and their ferroelectric and optical properties have been established. The Ba²⁺:Sr²⁺ ratio in these crystals was 6:0, 4:2, 3:3, and 2.5: 3.5. Although the growth of these crystals is extremely difficult due to the presence of Nb⁵⁺ and Ti⁴⁺ cations on the 6-fold coordinated sites, we have been successful in growing these tetragonal (4mm) crystals > 1.5 cm diameter with the Ba:Sr ratio of 4:2 and 3:3. These crystals exhibit high spontaneous polarization (> 30 $\mu\text{C}/\text{cm}^2$) and low dielectric constants (< 400), thus providing a high optical (r_{ij}/E) and piezoelectric (d_{33}/E) figures-of-merit. Ce-doped BSTN crystals have a fast photorefractive response and large two-beam coupling gain coefficient comparable to other bronze crystals such Sr_{1-x}Ba_xNb₂O₆ (SBN), Ba_{2-x}Sr_xK_{1-y}Na_yNb₅O₁₅ (BSKNN) and Sr_{2-x}Ca_xNaNb₅O₁₅ (SCNN), grown in our earlier work. Because of the low dielectric constant and high gain the optical figures-of-merit for BSTN is superior to SBN and BSKNN and as a result should find many applications.

INTRODUCTION

We are engaged in a systematic study of the photorefractive properties available in ferroelectric tungsten bronze and related systems (1-10). Our goal is to maximize both the photorefractive speed and gain in the desired spectral range. We have classified the tungsten bronze ferroelectrics into four categories based on their ferroelectric and optical characteristics as an aid in identifying the most promising candidates for photorefractive applications (11-15). Currently, we have begun exploring Ti^{4+} - containing bronze systems where photorefractive speed is potentially faster than in SBN while the two-beam coupling is comparable. These Ti^{4+} -containing tungsten bronzes are similar to the SBN solid solution crystals with respect to their ferroelectric and optical characteristics.

This paper reports the growth and material properties of Ti^{4+} -containing single crystals based on ferroelectric $(\text{Ba}, \text{Sr})_6\text{Ti}_2\text{Nb}_8\text{O}_{30}$ (BSTN) system. As shown in Figure 1, this solid solution exists on the $(1-x) \text{Ba}_6\text{Ti}_2\text{Nb}_8\text{O}_{30} - (x) \text{Sr}_6\text{Ti}_2\text{Nb}_8\text{O}_{30}$ system and our current work show a morphotropic phase boundary at $x \sim 0.70$ (16). On the BTN side of the phase diagram, the structure is tetragonal (4mm) whereas at the other side of MPB the structure is orthorhombic (mm2).

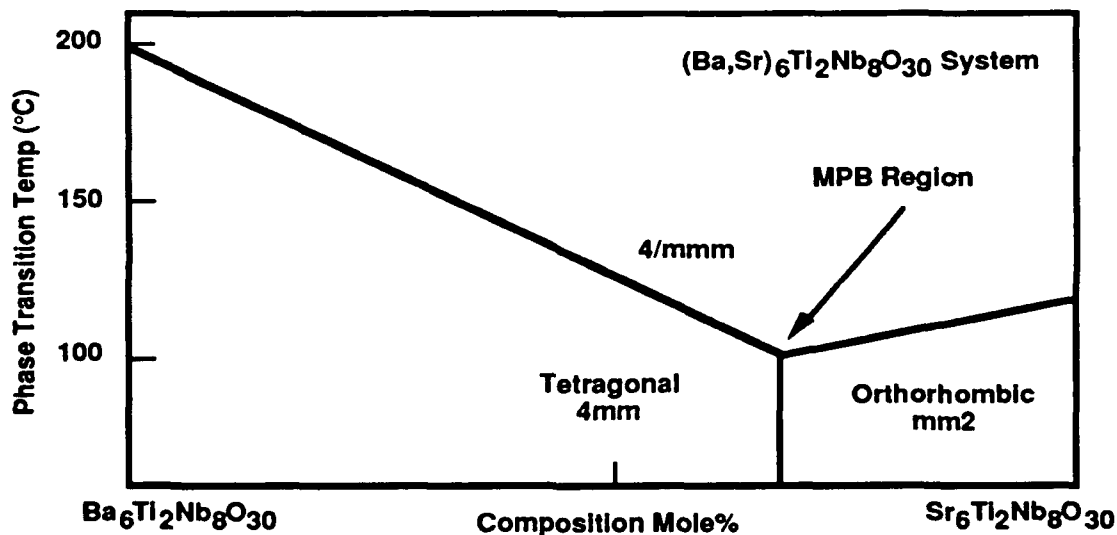


Figure 1 - Phase relation in the $\text{Ba}_6\text{Ti}_2\text{Nb}_8\text{O}_{30}$ - $\text{Sr}_6\text{Ti}_2\text{Nb}_8\text{O}_{30}$ system.

EXPERIMENTAL

The $(\text{Ba,Sr})_6\text{Ti}_2\text{Nb}_8\text{O}_{30}$ (BSTN) solid solution system was initially studied using reagent grade chemicals, specifically BaCO_3 , SrCO_3 , TiO_2 and Nb_2O_5 . The appropriate weighed materials were thoroughly mixed and calcined at 900°C and then sintered at 1250° to 1300°C . The structure identification and solid solubility range of tetragonal and orthorhombic structures were determined by x-ray diffraction measurements. The BSTN compositions were also studied using DTA techniques to ascertain melting temperature and supercooling range.

For single crystal growth experiments, high-purity starting materials (Johnson Matthey, Ltd.) were used. To maintain a high degree of homogeneity in the crystals, the starting materials were thoroughly ball-milled before melting in a platinum crucible. The crucible was 2" in both diameter and height, and was supported in a fibrous alumina insulting jacket. The furnace was rf induction-heated at 370 kHz. All crystals were cooled through their paraelectric/ferroelectric phase transition in an after-heater furnace.

A variety of techniques were used to evaluate the ferroelectric, pyroelectric and optical properties of these crystals. Prior to measurements, the crystals were poled at room temperature with a dc field of 8-10 kV/cm along the polar axis using either platinum or gold electrodes. The completeness of poling was checked by measuring the dielectric constant and piezoelectric d_{33} coefficient before and after poling.

RESULTS AND DISCUSSION

Table 1 lists the BSTN single crystals grown with their associated crystal growth conditions and lattice parameters. All BSTN single crystals were grown using an automatic diameter controlled (ADC) Czochralski technique used for other tetragonal and orthorhombic tungsten bronze crystals.

The growth conditions used were as follows:

- | | |
|----------------------|-------------------------------------|
| - Growth Temperature | $> 1480^\circ - 1500^\circ\text{C}$ |
| - Pulling Rate | 4-6 mm/hr |
| - Rotation Rate | 20-45 rpm |
| - Growth Atmosphere | Oxygen |
| - Cooling rate | $50-60^\circ/\text{h}$ |

- Growth Direction

Along the c-axis (using BSTN seed materials).

Table 1
Growth conditions and properties of BSTN single crystals

Composition	Growth Temp (°C)	Lattice Constant (Å)		Crystal Size (cm)
		a	c	
$\text{Ba}_6\text{Ti}_2\text{Nb}_8\text{O}_{30}$ (BTN)	1510	12.582	4.013	< 1.0
$\text{Ba}_4\text{Sr}_2\text{Nb}_8\text{O}_{30}$ (BSTN-1)	1490	12.501	3.985	> 1.5
$\text{Ba}_3\text{Sr}_3\text{Ti}_2\text{Nb}_8\text{O}_{30}$ (BSTN-2)	1485	12.478	3.968	> 1.5
$\text{Ba}_{2.5}\text{Sr}_{3.5}\text{Ti}_2\text{Nb}_8\text{O}_{30}$ (BSTN-3)	1480	12.455	3.952	~ 1.0
$\text{Ba}_2\text{Sr}_4\text{Ti}_2\text{Nb}_8\text{O}_{30}^*$ (BSTN-4)	1480	---	---	---
$\text{Sr}_6\text{Ti}_2\text{Nb}_8\text{O}_{30}^*$ (STN)	1500	---	---	---

* Compositions are orthorhombic and are difficult to grow.

Initially, undoped SBN:60 crystal seeds of optical quality were used for these growths; however, cracking of the boules was a severe problem during cool down. For this reason, we grew small BSTN seed materials using platinum wire and these seeds were used in subsequent growth experiments to reduce the cracking problem. BSTN-1 and BSTN-2 single crystals as large as 1.5 cm diameter and 5-7 cm long were grown along the (001) direction, as shown in Figure 2 for BSTN-2. $\text{Ba}_6\text{Ti}_2\text{Nb}_8\text{O}_{30}$ single crystals were not grown in this study, but the results reported in Table 1 are taken from the work of Ito et al (17-18). The other crystal compositions (BSTN-3, BSTN-4 and STN) were grown in small sizes. As the Sr^{2+} -concentration was increased, specifically in the orthorhombic BSTN or STN crystals, the growth became extremely difficult. Growth along other orientations, e.g. (100) and (110), was also tried, but the rate of crystallization along those directions was extremely slow. For this reason, all succeeding growth experiments were performed only along the (001) direction.

The Czochralski growth technique has been well developed for the growth of large size, optical quality tungsten bronze crystals within several systems such as $\text{Sr}_{1-x}\text{Ba}_x\text{Nb}_2\text{O}_6$ (SBN), $\text{Ba}_{2-x}\text{Sr}_x\text{K}_{1-y}\text{Na}_y\text{Nb}_5\text{O}_{15}$ (BSKNN) and $\text{Sr}_{2-x}\text{Ca}_x\text{NaNb}_5\text{O}_{15}$ (SCNN). Recently, we have been successful in growing SBN:60 crystals in excess of 5 cm diameter (19-25). All of these crystal

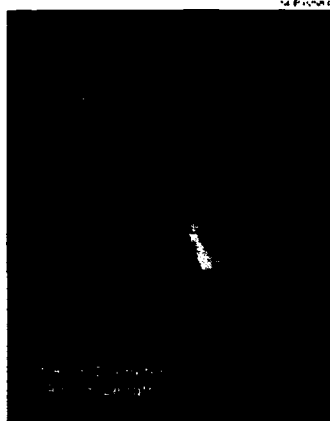


Figure 2 - Tungsten Bronze BSTN crystal boule grown along the (001) direction.

Table 2
Ferroelectric and optical properties of BSTN single crystals

Composition	T_c (°C)	Dielectric Constant (ϵ)	Polarization $\mu\text{C}/\text{cm}^2$	Electro-Optic Coeff $\times 10^{-12} \text{ m/V}(**)$	Piezo-Coeff pC/N
BTN	245	$\epsilon_{33} = 209$ $\epsilon_{11} = 193$	22	$r_{33} = 180$	---
BSTN-1	167	$\epsilon_{33} = 235$ $\epsilon_{11} = 182$	33.2	$r_{33} = 200$	$d_{33} = 95$
BSTN-2	170	$\epsilon_{33} = 270$ $\epsilon_{11} = --$	30.9	$r_{33} = 148$	$d_{33} = 104$
BSTN-3	118	$\epsilon_{33} = 345$ $\epsilon_1 = 248$	29.4	$r_{33} = 179$	$d_{33} = 125$
BSTN-4	95*	----	----	----	----
STN	110, 270*	$\epsilon_{33} = 320$	----	----	----

* Data is based on ceramic work (Ref. 16). ** Computed using equation 2.

The ferroelectric and optical properties of various BSTN crystals grown in this work are listed in Table 2. Figure 3 shows the weak-field c-axis dielectric constant, ϵ_{33} , for BSTN-3. This composition shows an extraordinarily sharp second order phase transition at $T_c = 118^\circ\text{C}$ where the dielectric peak exceeds 110,000, the highest value we have ever observed in a tungsten bronze

compositions are based on solid solution systems; hence the establishment of true congruent melting compositions within these systems is often difficult. Although we have suppressed various growth problems for the tungsten bronze crystals including BSTN, cracking still is a concern for BSTN crystals. The following two aspects seem to be responsible for this problem:

1. BSTN compositions are based on "filled" bronze structures i.e. both the 15- and 12-fold coordinated lattice sites are completely filled, whereas in the case of SBN these sites are partially empty.
2. The presence of two different cations, e.g. Nb^{5+} and Ti^{4+} on the 6-fold coordinated sites. This is the first example in our studies of a system having two different cations occupying the 6-fold coordinated sites.

The growth of BSTN single crystals is extremely difficult compared to other tungsten bronze crystals we have studied (). Since the Nb^{5+} and Ti^{4+} in BSTN cations are distributed over two 6-fold coordinated sites in tungsten bronze structure, it is important to establish their distribution in these sites (random or ordered). We have previously discussed that the quality of SBN crystals depends strongly on the distribution of Ba^{2+} and Sr^{2+} over the 15- and 12-fold coordinated sites (11-14). Generally, Ba^{2+} prefers the 15-fold coordinated site and Sr^{2+} the 12-fold coordinated site in tungsten bronze SBN structure, although Sr^{2+} also occupies some 15-fold coordinated sites. This distribution alters under different cooling conditions and thus introduces optical defects. To obtain optical quality , crack -free SBN crystals, the growth and cooling conditions must be carefully controlled to avoid the site exchanges which lead to these defects. For this reason, we need to know the role of the Nb^{5+} and Ti^{4+} cations and their distribution over the two 6-fold coordinated sites in BSTN crystals and this will allow us to reestablish the growth conditions to produce crack free and optical quality single crystals.

As shown in Figure 2, the growth habit of BSTN single crystals is similar to SBN with a cylindrical shape having 24 well-defined facets (11-14). As also seen in SBN crystals, the width of the (100) or (110) facets is always larger compared to other facets. Other example of this type are the tungsten bronze $\text{Sr}_2\text{KNb}_5\text{O}_{15}$ and $\text{Ba}_2\text{KNb}_5\text{O}_{15}$ crystals ().

ferroelectric crystal. Furthermore, unlike bronze SBN:60, dielectric relaxation effects are virtually absent in poled crystals over a 100 Hz - 100 kHz range except within 3-4° of T_c , as illustrated by the temperature dependence of the 10 kHz dielectric loss in Fig. 3. The absence of strong relaxor effects indicates that the cation site preferences remain consistent throughout the crystal bulk, resulting in an extremely narrow distribution of phase transition temperatures. Other BSTN compositions also show similar dielectric anomalies with low dispersion.

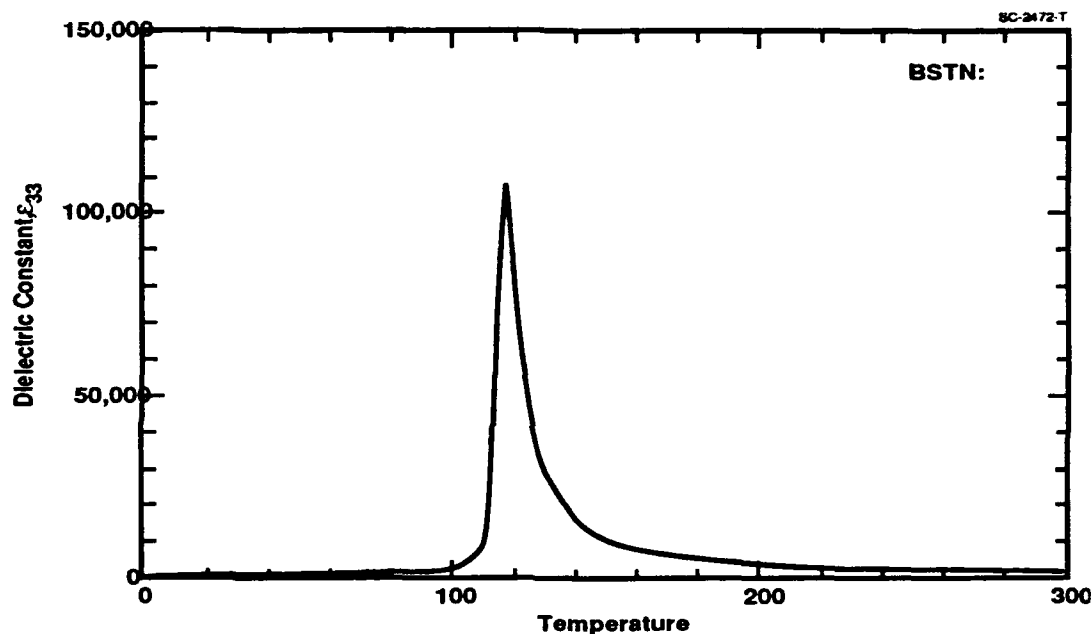


Figure 3 - Polar c-axis dielectric constant vs temperature for BSTN-3.

Figure 4 shows the temperature dependencies of the spontaneous polarization, P_3 , and the pyroelectric coefficient of BSTN-3. The room-temperature spontaneous polarization is $29.4 \mu\text{C}/\text{cm}^2$, slightly larger than in SBN:60 because of the higher phase transition temperature for BSTN-3.

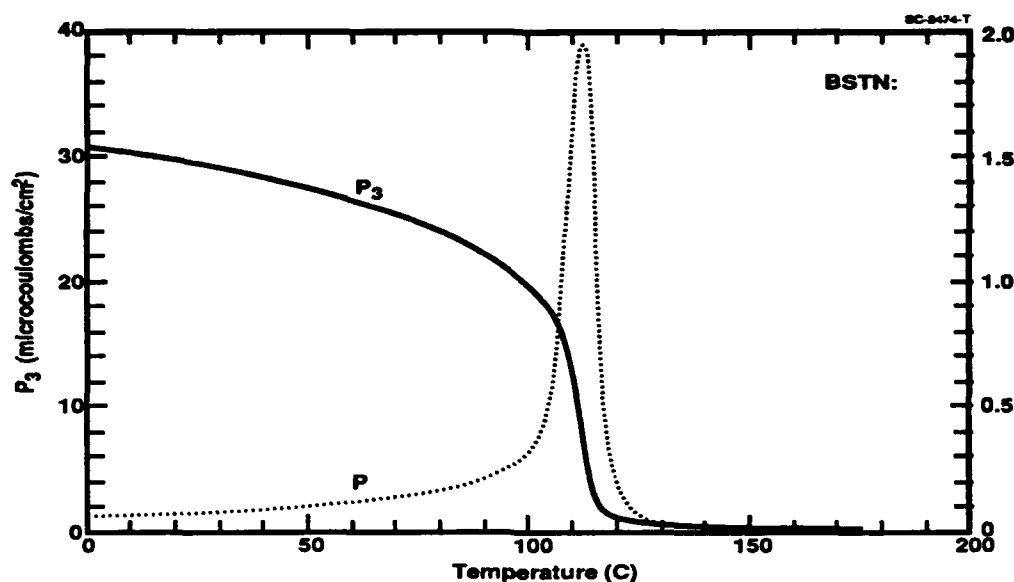


Figure 4 - Spontaneous polarization, P_3 , and pyroelectric coefficient, p , for BSTN-3.

The temperature dependencies of the non-polar a-axis dielectric constant, ϵ_{11} , and dielectric loss BSTN-3 are shown in Figure 5. The room-temperature dielectric constant is 248, roughly 1/2 the value found in SBN:60, while the dielectric losses are extraordinarily low, being less than 0.003 at room temperature over a 100 Hz - 100 kHz range, and dropping below 0.0002 above T_c . This behavior suggests that the losses below T_c are associated with a slight tilting of the polar vector, P_3 , with the application of an electric field orthogonal to the c-axis, a phenomenon which has also been postulated in the SBN bronzes on the basis of millimeter wave properties (). Figures 6 and 7, show the behavior of the ac conductivities with reciprocal temperature for a- and c-axis Ce-doped BSTN-3. Note again the very sharp behavior of the conductivity just below T_c for the c direction. At a temperature above 300°C the conductivity becomes non-dispersive down to dc with an n-type thermal activation energy of 1.29 eV; this is presumably the position of the Ce^{3+} donor level, although more work will be necessary to confirm this.

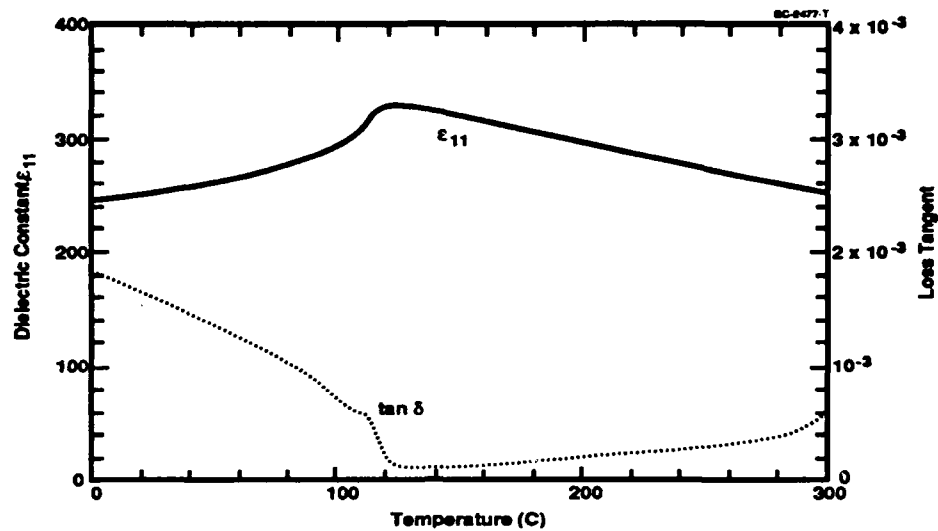


Figure 5 - Non-polar a-axis dielectric constant and loss vs temperature for BSTN-3.

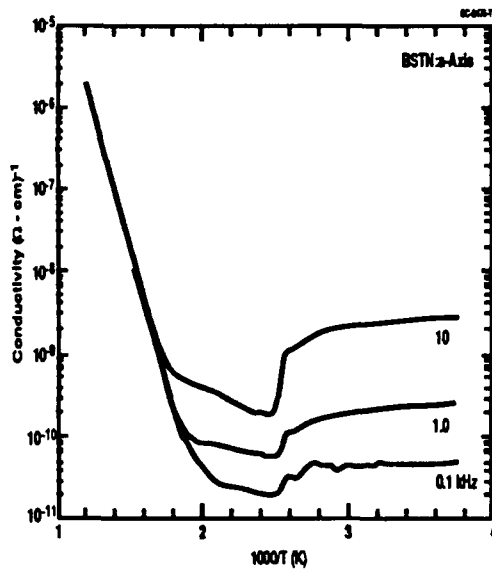


Figure 6 - Non-polar a-axis ac conductivity for BSTN-3.

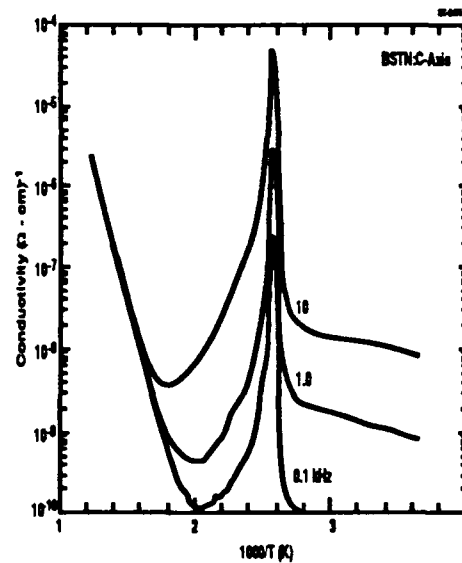


Figure 7 - Polar c-axis ac conductivity for BSTN-3.

Table 2 summarizes the major properties of BSTN crystals. One property of major importance in the Table is the high value for the piezoelectric coefficient d_{33} (125 pC/N). From the phenomenology for bronze ferroelectrics, d_{33} is given by

$$d_{33} = 2Q_{33}P_3\epsilon_{33}\epsilon_0 \text{ ----- (1)}$$

where Q_{33} is the electrostrictive coefficient. Typically, Q_{33} has a value of roughly $0.035 \text{ m}^4/\text{C}^2$ (e.g., SBN) which has been found to be largely invariant across the range of possible tungsten bronze ferroelectric oxides. However, in the case of BSTN-3, Q_{33} is nearly twice as large at $0.069 \text{ m}^4/\text{C}^2$, with the resulting piezoelectric figure-of-merit, d_{33}/ϵ_{33} , also being twice that of SBN:60. This is important for electro-optical and photorefractive applications because of the similarity of the phenomenological expressions for the linear electro-optic constants, e.g.,

$$r_{33} = 2g_{33}P_3\epsilon_{33}\epsilon_0 \text{ ----- (2)}$$

Where g_{33} is the transverse quadratic electro-optic coefficient, $g_{33} \sim 0.1 \text{ m}^4/\text{C}^2$ for tungsten bronze crystals. There is evidence in the BSKNN system that g is proportional to Q (). A factor of 2 increase in Q should lead to a corresponding increase in g for BSTN crystals. Therefore we expect that BSTN crystals will also have twice the anticipated r_{33} (and r_{51}) and electro-optic figures-of-merit up to a factor two larger than in SBN-type crystals.

As seen in Table 2, the computed transverse (r_{33}) electro-optic and the measured piezoelectric strain coefficient (d_{33}) increased with increasing Sr^{2+} concentration in BSTN up to the MPB region. Both optical (r_{ij}/ϵ) and piezoelectric (d_{33}/ϵ) figures-of-merit are largest for BSTN-1 crystal. However, these differences in figures-of-merit are small, and all of these BSTN crystal compositions are excellent choices for both optical and piezoelectric applications. We are currently attempting to grow orthorhombic BSTN as well as $\text{Sr}_6\text{Ti}_2\text{Nb}_8\text{O}_{30}$ (STN), and we expect both the transverse (r_{33}) and longitudinal (r_{51}) electro-optic coefficients will be very large near the MPB region.

PHOTOREFRACTIVE PROPERTIES

The photorefractive properties Ce-doped BSTN-1 have recently been determined by Wood et al (26) with a cube and plate having dimensions of $5 \times 5 \times 5 \text{ mm}$ and $5 \times 5 \times 1 \text{ mm}$, respectively. The properties have been derived from two-beam coupling measurements and they are similar to Ce-doped SBN:60. The concentration of $\text{Ce}^{3+}/\text{Ce}^{4+}$ in BSTN crystal is 0.02 wt% with a linear absorption at 488 nm of $\alpha = 2.45 \text{ cm}^{-1}$. The effective density of charge at this dopant concentration was measured to be $6.4 \times 10^{16} \text{ cm}^{-3}$. This density yielded an inverse Debye screening length of $k_0^{-1} = 87 \text{ nm}$. The dominant charge carrier was found to be electrons. By assuming the predicted

electro-optic coefficients, the electron-hole competition factor was measured to be $\xi = 0.5$, indicating 3 times more electrons are participating in charge diffusion than holes. The largest two beam coupling gain coefficient measured with extraordinary polarization to take advantage of the large r_{33} was $\Gamma \sim 21 \text{ cm}^{-1}$. The time response was found to be exponential and inversely proportional to the incident intensity indicating a single active trap level and incident intensities above the decay rate due to the dark current. The time response was found to be $\tau_{1/e} = 0.102/I^{0.969}$, where I is given in W/cm^2 and $\tau_{1/e}$ is in seconds. From the time response it was determined that the charge transport length is $L_D = 128 \text{ nm}$.

Ce-doped SBN:60 and BSTN-1 show similar gain for the same effective charge density; however, the BSTN-1 needed to be doped higher resulting in a larger absorption in order to achieve the same charge density levels. At 1 W/cm^2 the measured values of the two-beam coupling response for BSTN-1 is 0.1 second (26) and can be compared to the measured value for SBN:60 of 0.3 second²⁷ where both crystals had approximately the same effective charge density. This observation indicates that Ce-doped BSTN has a 3x faster response and a coupling constant comparable to Ce-doped SBN:60 with the same level of effective charge carriers.

BSTN crystals have a filled tungsten bronze structure and show piezoelectric figure-of-merit d_{33}/ϵ_{33} which is approximately two times higher than SBN:60. We anticipate that the electro-optic figure-of-merit ($n^3 r_{ij}/\epsilon$) is proportionately larger than SBN:60, but accurate measurements of the linear electro-optic is currently underway. These crystals also show very sharp phase transition behavior compared to the relaxor behavior found in SBN. However, the photorefractive measurements strongly indicate that substantially high optical figure-of-merit for these crystals with photorefractive response speed at least 3 times faster than SBN for the same effective charge density. These preliminary results indicate that by optimizing the dopant valence states and their concentrations, the photorefractive speed and coupling should improve considerably.

Because BSTN has a filled tungsten bronze structure, its optical damage threshold should be considerably higher as seen in other filled tungsten bronze BSKNN and $\text{K}_3\text{Li}_2\text{Nb}_5\text{O}_{15}$ (). Dark conductivities are anticipated to be superior to SBN type crystals due to the filled structure and reduced structural defects. These preliminary results are very promising for possible use in optical computing and laser hardening applications. Our current goal is now to increase crystal size and dopant optimization in these crystals.

CONCLUSIONS

Ferroelectric tungsten bronze single crystals based on the $(\text{Ba,Sr})_6\text{Ti}_2\text{Nb}_8\text{O}_{30}$ system have been grown by the Czochralski technique and their ferroelectric and optical properties have been established. These crystals exhibit high spontaneous polarization ($> 30 \mu\text{C}/\text{cm}^2$) and low dielectric constants (< 400), thus providing a high optical (r_{ij}/ϵ) and piezoelectric (d_{33}/ϵ) figures-of-merit. Ce-doped BSTN crystals have a fast photorefractive response and large two-beam coupling gain coefficient comparable to other bronze crystals such $\text{Sr}_{1-x}\text{Ba}_x\text{Nb}_2\text{O}_6$ (SBN), $\text{Ba}_{2-x}\text{Sr}_x\text{K}_{1-y}\text{Na}_y\text{Nb}_5\text{O}_{15}$ (BSKNN) and $\text{Sr}_{2-x}\text{Ca}_x\text{NaNb}_5\text{O}_{15}$ (SCNN), grown in our earlier work. Because of the low dielectric constant and high gain the optical figures-of-merit for BSTN is superior to SBN and BSKNN and as a result should find many applications.

ACKNOWLEDGEMENTS

This work was supported by DARPA (F49620-90-C-0089) and Rockwell International Research and Development funding. The authors thank Professor L. E. Cross of the Pennsylvania State University for his useful suggestions during the course of this work.

REFERENCES

1. G.J. Salamo, M.J. Miller, W.W. Clark III, G.L. Wood, E.J. Sharp and R.R. Neurgaonkar, *Appl. Optics* **27**(21), 4356 (1988).
2. E.J. Sharp, M.J. Miller, G.J. Salamo, W.W. Clark III, G.L. Wood, and R.R. Neurgaonkar, *Ferroelectrics* **87**, 335 (1988).
3. K. Sayano, G.A. Rakuljic, A. Agranat, A. Yariv and R.R. Neurgaonkar, *Optics. Lett.* **14**(9), 459 (1989).
4. J. Ford, Y. Taketomi, S. Lee, D. Bize, S. Feinman and R.R. Neurgaonkar, *Proc. SPIE* **1148**, 12 (1989).
5. G. L. Wood, W. W. Clark III, G. J. Salamo, A. Mott and E. J. Sharp, *J. Appl. Phys.* **71**, 37 (1992).
6. E. J. Sharp, M. J. Miller, G. J. Salamo, W. W. Clark III, G. L. Wood, and R. R. Neurgaonkar, *Ferroelectrics* **87**, 335 (1988).
7. E. J. Sharp, G. L. Wood, W. W. Clark III, G. J. Salamo and R. R. Neurgaonkar, *Opt. Lett.*

17, 207 (1992).

8. S. G. Rabbani, J. L. Shultz, G. J. Salamo, E. J. Sharp, W. W. Clark III, M. J. Miller, G. L. Wood and R. R. Neurgaonkar, Appl. Phys. B53, 323 (1991).
9. E. J. Sharp, W. W. Clark III, M. J. Miller, G. L. Wood, B. Monson, G. J. Salamo and R. R. Neurgaonkar, Appl. Opt. 29, 743 (1990).
10. G. J. Salamo, M. J. Miller, W. W. Clark III, G. L. Wood, E. J. Sharp and R. R. Neurgaonkar, Appl. Opt. 27, 4356 (1988).
11. R.R. Neurgaonkar and W.K. Cory, J. Opt. Soc. Am. 3(B), 276 (1986).
12. R.R. Neurgaonkar, W.K. Cory, J.R. Oliver, M.D. Ewbank and W.F. Hall, J. Opt. Eng. 26(5), 392 (1987).
13. R. R. Neurgaonkar, W. K. Cory, J. R. Oliver, M. Khoshnevisan and E. J. Sharp, Ferroelectrics 102, 3 (1990).
14. R. R. Neurgaonkar, W. F. Hall, J. R. Oliver and W. K. Cory,
15. R. R. Neurgaonkar, W. K. Cory, J. R. Oliver, E.J. Sharp, G. L. Wood and G. J. Salamo, To be published Special Issue of Ferroelectrics, 1993.
16. R. R. Neurgaonkar, J.G. Nelson and J. R. Oliver, Mat. Res. Bull. 26, 234 (1991).
17. Y. Ito and H. Iwasaki, J. Phys. Chem. Solids 34, 1639 (1973).
18. Y. Ito, S. Miyazawa, T. Yamada and H. Iwasaki, Jap. J. Appl. Phys. 9, 157 (1970).
19. R.R. Neurgaonkar, W.K. Cory, J.R. Oliver, E.J. Sharp, G.L. Wood, M.S. Miller, W.W. Clark III and G. Salamo, Mat. Res. Bull. 23, 1459 (1988).
20. R.R. Neurgaonkar, W.K. Cory, J.R. Oliver, M.J. Miller, W.W. Clark III, G.L. Wood, and E.J. Sharp, J. Cryst. Growth 84, 629 (1987).
21. R.R. Neurgaonkar, W.K. Cory, W.W. Ho, W.F. Hall, and L.E. Cross, Ferroelectrics 38, 857 (1981).
22. R.R. Neurgaonkar, W.K. Cory, W.W. Ho, W.F. Hall, and L.E. Cross, Ferroelectrics 38, 857 (1981).
23. R.R. Neurgaonkar, W.K. Cory, J.R. Oliver and L.E. Cross, Mat. Res. Bull. 24, 1025 (1989).
24. R. R. Neurgaonkar, W. K. Cory, J. R. Oliver and L. E. Cross, J. Cryst. Growth 89, 463 (1988).
25. R. R. Neurgaonkar, W. K. Cory, J. R. Oliver, E. J. Sharp, G. L. Wood, M. J. Miller, W. W. Clark III and G. J. Salamo, Mat. Res. Bull. 23, 1459 (1988).



Rockwell International

Science Center

SC71041.FR

APPENDIX 6.2

FERROELECTRIC PROPERTIES OF $(\text{BaSr})_6\text{Ti}_2\text{Nb}_8\text{O}_{30}$ SINGLE CRYSTALS

FERROELECTRIC PROPERTIES OF $(\text{Ba}_{1-x}\text{Sr}_x)_6\text{Ti}_2\text{Nb}_8\text{O}_{30}$ (BSTN) SINGLE CRYSTALS

John R. Oliver and Ratnakar R. Neurgaonkar

Rockwell International Science Center

Thousand Oaks, California USA 91360

INTRODUCTION

In the tungsten bronze $(\text{Ba}_{1-x}\text{Sr}_x)_6\text{Ti}_2\text{Nb}_8\text{O}_{30}$ (BSTN) system, the partial substitution of Ti^{4+} for Nb^{5+} in the 6-fold coordinated lattice sites permits all of the 15- and 12-fold sites to be filled by Sr^{2+} and Ba^{2+} in what would otherwise be a partially-filled $\text{Sr}_{1-x}\text{Ba}_x\text{Nb}_2\text{O}_6$ (SBN) type structure. The combination of a filled structure and the lower valence state of Ti encourages any dopant ions to thus occupy the lower 9- and 6-fold lattice sites with the potential for photorefractive spectral responses extending to the near-IR region.

An interesting feature of BSTN is that it is ferroelectric at both end members of the pseudo-binary phase diagram ($x = 0, 1$), unlike the SBN system. Figure 1 shows the behavior of the ferroelectric phase transition temperature, T_c , determined from dielectric data on ceramic compositions. Note that T_c does not decline monotonically with increasing Sr content, but instead has a minimum in the vicinity of $x = 0.70$, suggesting the presence of a morphotropic phase boundary where tetragonal and weakly orthorhombic phases may coexist. In this paper, we describe the results for three tetragonal BSTN compositions grown as bulk single crystals using the Czochralski technique.

EXPERIMENTAL RESULTS

We initiated the Czochralski crystal growths of several BSTN compositions in Ce-doped form after first investigating the growth of undoped compositions. These crystals were pulled from platinum crucibles at 1470 - 1475°C using a Czochralski puller with automatic diameter control to insure tight compositional control. We initially used $\langle 001 \rangle$ oriented SBN:60 crystals as seeds for these growths, but with continued crystal growth work we now have BSTN crystals of sufficient

quality to use as seed material; this has helped to improve the overall quality of the more recently grown crystals.

Of the BSTN compositions investigated, the most recently grown composition, BSTN:38 (Ba:Sr = 38:62), has been the easiest to grow as fracture-free crystal boules, indicating that this composition may lie at or near the congruent melting region of the phase diagram. If the latter ultimately proves to be the case, this would make the congruently melting Ba:Sr ratio for BSTN nearly identical to that of the congruently melting SBN:61.

Among the doped crystals, our work has focused primarily on Ce-doped BSTN:42 which has a ferroelectric phase transition at $T_c = 116^\circ\text{C}$. Figure 2 shows the weak-field c-axis dielectric constant, ϵ_{33} , as a function of temperature for an unannealed and annealed (700°C for 3 hours in O_2) Ce-doped (0.01 wt%) BSTN:42 crystal sample poled at room temperature with a dc field of 10 kV/cm. BSTN:42 shows a characteristically sharp second-order phase transition at T_c with the dielectric peak exceeding 100,000, the largest value we have ever observed in tungsten bronze ferroelectric crystals. Also shown in the figure is the dielectric behavior of the same crystal prior to annealing. Unlike tungsten bronze SBN:60, dielectric relaxation effects along the c-axis are virtually absent in poled crystals over a 100 Hz - 100 kHz range except within a $3 - 5^\circ$ range of T_c , and the room-temperature dielectric losses are typically less than 0.005 above 1 kHz. The absence of strong relaxor effects indicates that the ionic site preferences remain fairly consistent throughout the crystal bulk, resulting in an extremely narrow distribution of phase transition temperatures. This behavior suggests the use of these crystals in high-frequency applications, perhaps up to millimeter wave frequencies (e.g., phase shifters) where SBN:60 has been found unsuitable due to high dielectric losses. However, indications from other BSTN crystal compositions are that the dielectric losses near T_c increase with lower Ba:Sr ratios, reflecting broader phase transition distributions in these compositions.

Figure 3 shows the temperature dependencies of the spontaneous polarization, P_3 , and the pyroelectric coefficient for Ce-doped BSTN:42. The room-temperature spontaneous polarization is $29.2 \mu\text{Coulombs}/\text{cm}^2$, slightly larger than in SBN:60 because of the higher phase transition temperature for BSTN:42. Similar to bronzes such as SBN and BSKNN, the polarization over a 150° range below T_c follows a temperature dependence given by

$$P_3 = P_{s0}(\Theta_{3f} - T)^{(1/6)},$$

where Θ_{3f} ($= T_c$) is the Curie temperature of the ferroelectric phase. As discussed later, Θ_{3f} is not necessarily equal to the paraelectric Curie temperature, Θ_3 .

The temperature dependencies of the non-polar a-axis dielectric constant, ϵ_{11} , and dielectric loss are shown in Fig. 4. The room-temperature dielectric constant is $\epsilon_{11} = 260$, roughly 1/2 the value found in SBN:60, while the dielectric losses are extraordinarily low, being less than 0.003 at room temperature over a 100 Hz - 100 kHz range. These losses drop below 0.0002 above T_c , suggesting that the losses below T_c are associated with a slight tilting of the polar vector, P_3 , with the application of an electric field orthogonal to the c-axis, a phenomenon which has been postulated in the SBN bronzes on the basis of millimeter wave properties.

Figure 5 shows the behavior of the 100 Hz - 10 kHz ac conductivities with reciprocal temperature for c-axis Ce-doped BSTN:42. Note the very sharp behavior of the conductivity just below T_c . At temperatures above 350°C, the conductivity becomes non-dispersive down to dc with an n-type activation energy of 1.32 eV. This value is consistent with that in Ce-doped BSKNN crystals, and is presumably due to the Ce^{3+} donor level since the Fermi level in undoped crystals is pinned at the 1.6 eV Nb^{4+} mid-gap donor/recombination level. Along the non-polar a-axis, where dc measurements are not affected by pyroelectric currents, the dc conductivity (Fig. 6) shows strictly Arrhenius behavior over seven decades with an activation energy $E_a = 1.35$ eV, deviating from linearity only at the low-temperature end where $d\epsilon/dT$ effects influence the measurement. The slight difference in activation energies for the two axial directions can be attributed to a difference in the power-law temperature dependencies of the electron mobilities, since these necessarily make small contributions to the measured E_a values. For BSTN:42, the ratio of orthogonal mobilities $\mu_c/\mu_a = 2.6$ to 1.7 up to 600°C.

Table 1 summarizes the major properties of Ce-doped BSTN:42 along with two other Ce-doped compositions, BSTN:50 and BSTN:38. One property of particular importance in the Table are the high values for the piezoelectric coefficient d_{33} . From the phenomenology for bronze ferroelectrics, d_{33} is given by

$$d_{33} = 2Q_{33}P_3\epsilon_{33}\epsilon_0,$$

where Q_{33} is the quadratic electrostriction coefficient and ϵ_0 is the permittivity of free space. Typically, Q_{33} has a value of roughly 0.35 m⁴/C² (e.g., SBN compositions) among many of the

tungsten bronze ferroelectrics. However, in the case of BSTN:42 with $d_{33} = 125 \text{ pC/N}$, Q_{33} is nearly twice as large at $0.68 \text{ m}^4/\text{C}^2$, with the resulting piezoelectric figure-of-merit, d_{33}/ϵ_{33} , also being twice that of SBN:60. This is important for electro-optical and photorefractive applications because of the similarity of the phenomenological expressions for the linear electro-optic constants, e.g.,

$$r_{33} = 2g_{33}P_3\epsilon_{33}\epsilon_0,$$

where g_{33} is the transverse quadratic electro-optic coefficient. Our previous results with BSKNN-2 crystals have shown these to have r_{33} values roughly twice as large (160 - 180 pm/V) as one would predict from the above based on a g_{33} of $\sim 0.10 \text{ m}^4/\text{C}^2$. Similarly, BSKNN-2 crystals also have an effective Q_{33} , and piezoelectric figure-of-merit, which are comparable to the large values found in BSTN:42. Based on measurements on BSKNN and SBN crystals, we expect that the r coefficients for BSTN will scale with the piezoelectric d coefficients as $r \sim 2d$; thus, we anticipate that BSTN:42 crystals will also have unusually large values for r_{33} (and, r_{51}) and electro-optic figures-of-merit which are roughly a factor of two larger than in SBN-type crystals. The computed electro-optic values are shown in Table 1 for each BSTN composition based on their respective measured d_{33} coefficients.

A significant trend in Table 1 is the decline of the electrostriction constants and the figures-of-merit with decreasing Ba:Sr ratios; this is particularly evident with BSTN:38. This crystal also shows a more broadened phase transition compared to the other crystal compositions; this is evident from the plot of the dielectric stiffness as a function of temperature shown in Fig. 7. Considering the Curie-Weiss behavior of the dielectric constant in the paraelectric phase well above T_c ,

$$\epsilon_{33} = C_3/(T - \Theta_3),$$

it is seen from the figure that the extrapolated value of $\Theta_3 = 144^\circ\text{C}$ is 48° greater than T_c in BSTN:38. This behavior is quite similar to what is found in tungsten bronze SBN:60. What is especially interesting about the BSTN system is that the difference between Θ_3 and T_c decreases with increasing Ba content due to the fact that Θ_3 changes very slowly compared to T_c . For

example, for BSTN:50, Θ_3 is only 9° above T_c at 153°C, and the dielectric stiffness shows nearly ideal linear behavior with temperature both above and below T_c .

Ce-doped BSTN crystals show low room temperature dark conductivities of typically 10^{-15} ohm⁻¹-cm⁻¹ or better, but there is certainly room for further improvement based on prior experience with undoped SBN:60. Since the dopant level lies energetically deep in the band gap, any increased room-temperature conductivity primarily arises from the presence of shallow defect and impurity levels, including vacancies, since the presence of only the compensated 1.32 eV Ce³⁺ donor would result in a dark conductivities at room temperature of approximately 4×10^{-20} ohm⁻¹-cm⁻¹. Hence, continued progress with the purity of the starting materials and evolutionary improvements in the growth technique should contribute to substantially lower room-temperature conductivities in these crystals with a corresponding increase in the image retention time in holographic applications.

CONCLUSIONS

Based on the excellent ferroelectric properties of these new crystals, we feel that BSTN:42, and perhaps other future BSTN compositions, could have a very important role in high figure-of-merit electro-optic and photorefractive applications. Work remains, however, to further improve the optical quality of these crystals, particularly regarding the suppression of optical striations, and to reduce the concentration of shallow impurity and defect levels.

Table 1
Ferroelectric Properties of Ce-Doped BSTN Crystals

	BSTN:50	BSTN:42	BSTN:38
T_c (°C)	143	116	96
At 23°C			
ϵ_{11}	----	260	275
ϵ_{33}	270	360	540
$\tan \delta$	<0.005	<0.003	<0.002
P_3 (C/cm ²)	30.9	29.2	7.0
d_{33} (pC/N)	103	125	142
Q_{33} (m ⁴ /C ²)	0.070	0.068	0.055
d_{33}/ϵ_{33}	0.381	0.347	0.263
r_{33} (pm/V)*	205	250	285
r_{33}/ϵ_{33} *	0.76	0.69	0.53

* Computed values based on $r_{33} \sim 2d_{33}$.

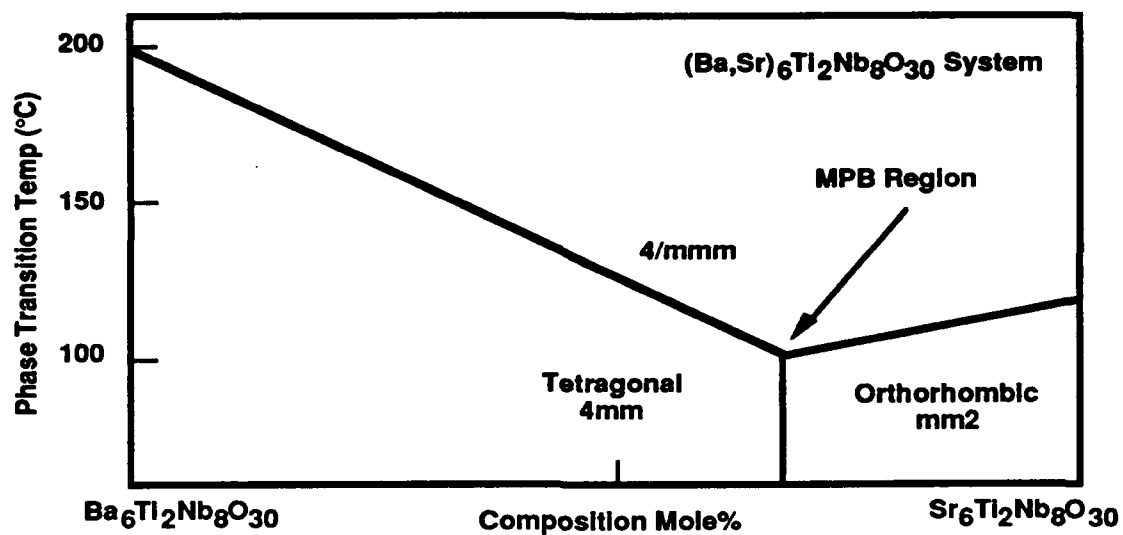


Figure 1 -- Phase diagram for the tungsten bronze BSTN system.

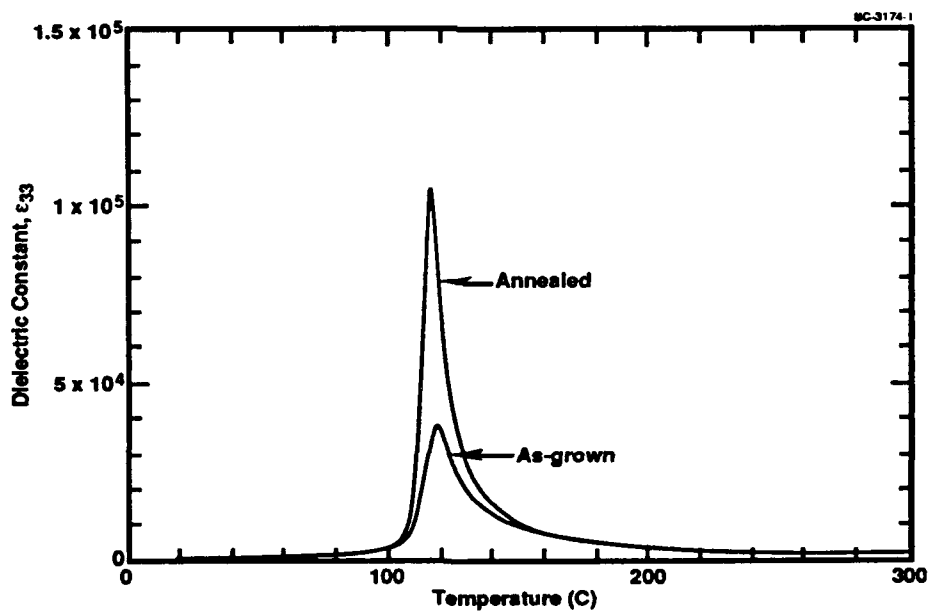


Figure 2 -- Polar axis dielectric constant vs temperature for a Ce-doped BSTN:42 crystal. Sample was annealed at 700°C for 3 hours in O_2 .

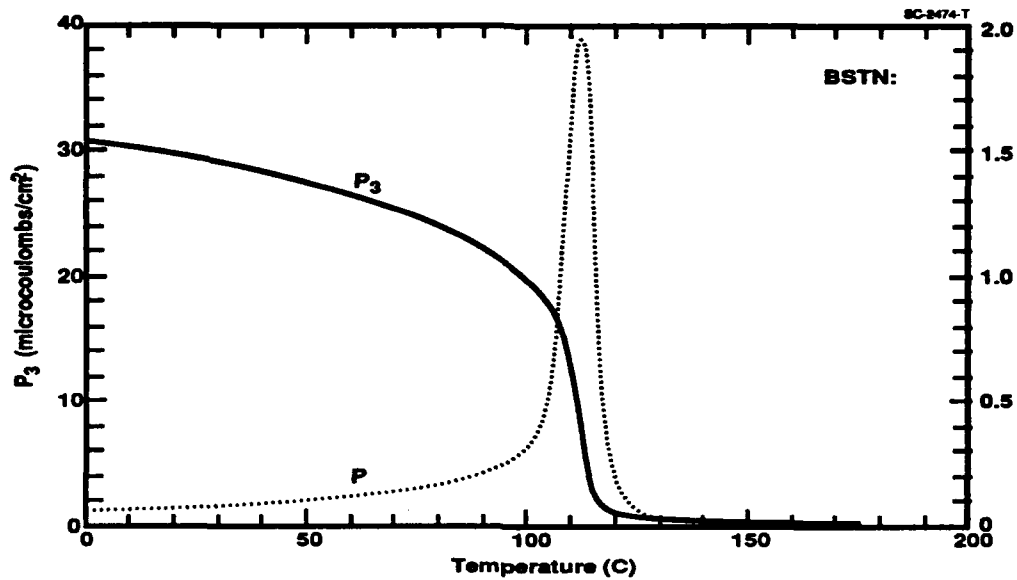


Figure 3 -- Spontaneous polarization, P_3 , and pyroelectric coefficient, p , vs temperature for Ce-doped BSTN:42.

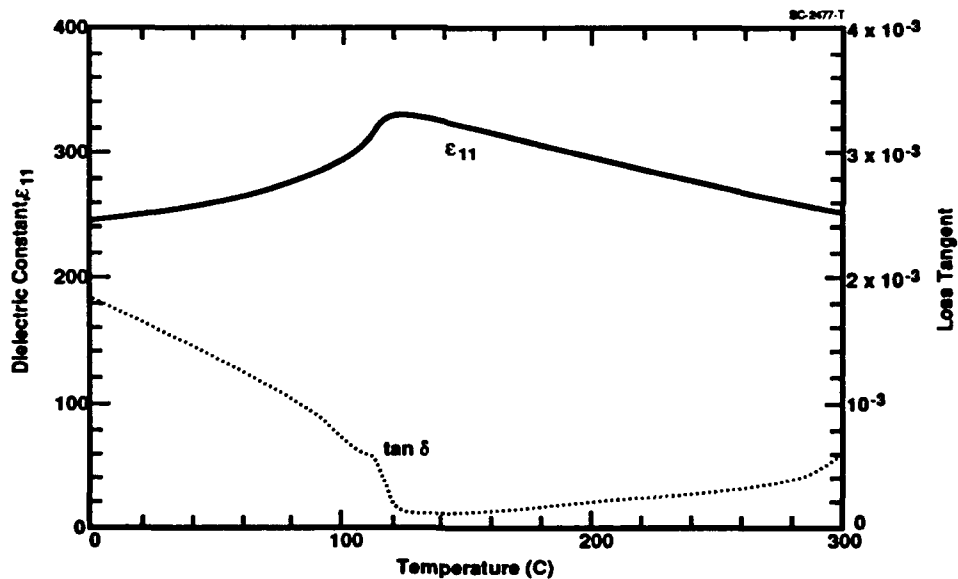


Figure 4 -- Non-polar a-axis dielectric constant and dielectric loss vs temperature for BSTN:42.

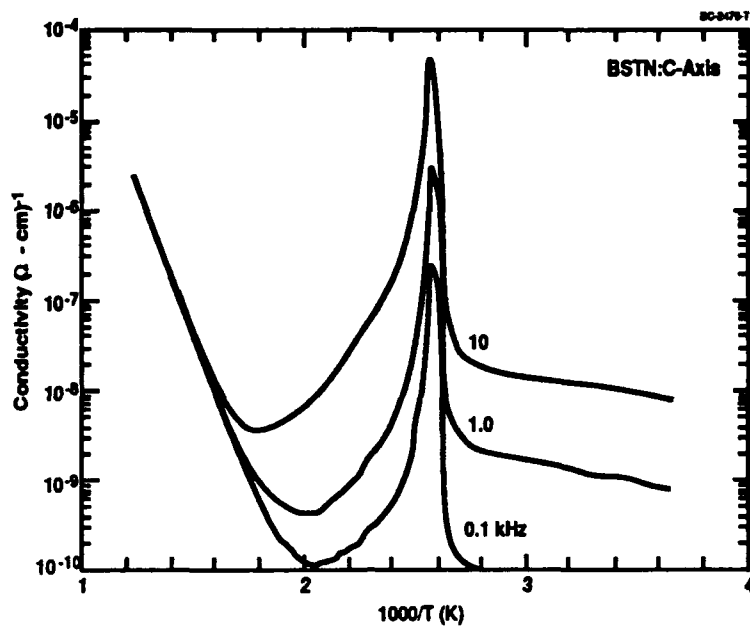


Figure 5 -- AC conductivity vs reciprocal temperature for Ce-doped BSTN:42.
 $f = 0.1, 1.0$ and 10 kHz .

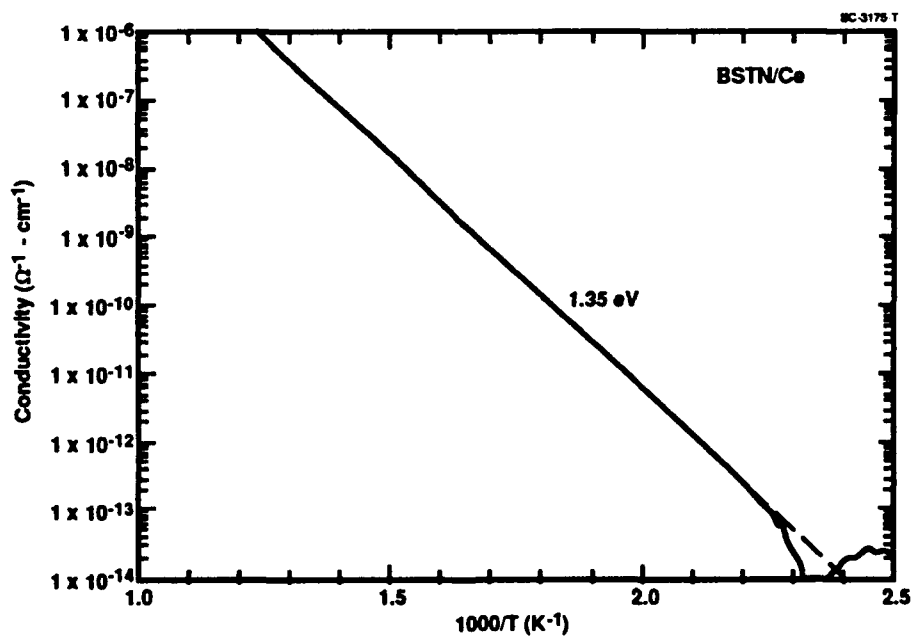


Figure 6 -- A-axis dc conductivity vs reciprocal temperature for Ce-doped BSTN:42.
 $E_a = 1.35 \text{ eV}$.

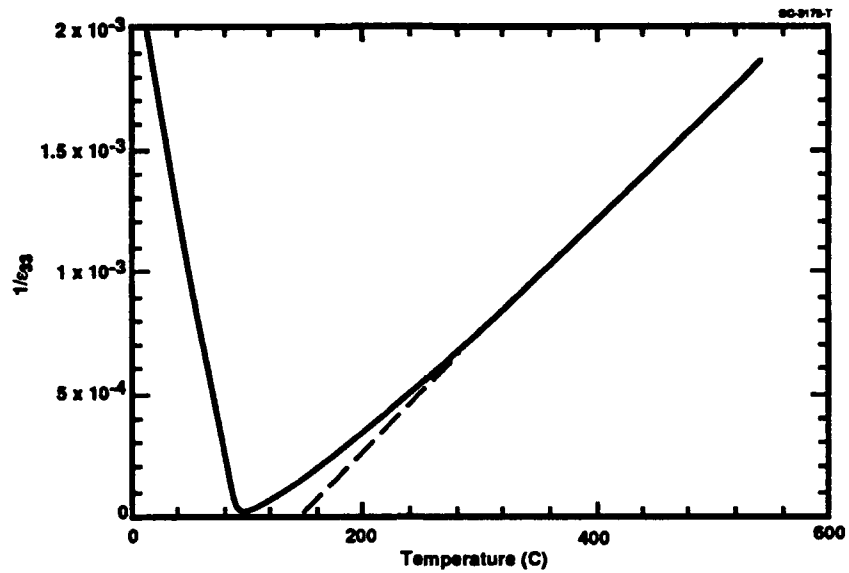


Figure 7 -- 100 kHz dielectric stiffness vs temperature for BSTN:38. Note the deviation from linearity below 280°C in the paraelectric phase.



Rockwell International

Science Center

SC71041.FR

APPENDIX 6.3

ELECTRICAL FIXING OF PHOTOREFRACTIVE HOLOGRAMS IN SBN:75

Electrical fixing of photorefractive holograms in $\text{Sr}_{0.75}\text{Ba}_{0.25}\text{Nb}_2\text{O}_6$

Yong Qiao, Sergei Orlov, and Demetri Psaltis

Department of Electrical Engineering, California Institute of Technology, Pasadena, California 91125

Ratnakar R. Neurgaonkar

Rockwell International Science Center, 1049 Camino dos Rios, Thousand Oaks, California 91360

Received February 1, 1993

Photorefractive holograms stored in $\text{Sr}_{0.75}\text{Ba}_{0.25}\text{Nb}_2\text{O}_6$ crystals are electrically fixed at room temperature. The fixed holograms can be read out directly or after a positive-voltage pulse is applied that can dramatically enhance the diffraction efficiency. Single gratings as well as images are recorded and fixed.

Volume holograms recorded in photorefractive materials can find important applications in optical memories and optical computing systems. One problem with a photorefractive hologram is that it gets erased by the readout light. Nondestructive readout can be achieved by hologram fixing, and several fixing methods have been reported. Thermal fixing of holograms was demonstrated in LiNbO_3 ,¹ $\text{Bi}_{12}\text{SiO}_{20}$,² KNbO_3 ,³ and BaTiO_3 ,⁴ where a compensating ionic charge grating (which cannot be erased optically) is formed at an elevated crystal temperature. Micheron and Bismuth demonstrated hologram fixing in $\text{Sr}_{0.75}\text{Ba}_{0.25}\text{Nb}_2\text{O}_6$ (Ref. 5; SBN:75) and BaTiO_3 (Ref. 6) through the creation of a ferroelectric domain pattern by applying an external field at room temperature. Hologram fixing in SBN:75 was also achieved by cooling the exposed crystal through the ferroelectric phase transition.⁷ Leyva *et al.* demonstrated hologram fixing in $\text{KTA}_{1-x}\text{Nb}_2\text{O}_6$ by cooling the exposed crystal under an applied field through the ferroelectric phase transition.⁸ In general, electrical fixing is preferable from a practical point of view because of its relative simplicity.

In this Letter we report the results of our investigation on electrical fixing of photorefractive holograms recorded in SBN:75. We were able to reproduce some of the effects that Micheron and Bismuth reported in Ref. 5, but our observations were different in several important respects. In addition, we report two novel ways of electrically fixing holograms in SBN:75 that give improved performance and demonstrated that holograms of images can be fixed and faithfully reproduced.

The crystal sample used in the experiment was grown and poled at Rockwell International Science Center. It has dimensions of 6 mm \times 6 mm \times 6 mm, with its *c* axis parallel to the edges. An external electric field can be applied along the *c* axis, and it is called positive (negative) if its direction is same as (opposite) that of the initial poling field. In our experimental setup (Fig. 1), an ordinary-polarized plane wave from an argon laser ($\lambda = 488$ nm) is split into three beams, two of which are used for recording a

grating in the crystal, with the third used as a non-Bragg-matched erasing beam. The grating vectors are approximately parallel to the *c* axis and the total recording intensity is ~ 10 mW/cm². The diffraction efficiency η is monitored with a low-intensity, extraordinary-polarized He-Ne laser beam incident at the Bragg angle. The diffraction efficiency is calculated by subtracting the background noise level from the measured diffracted light and dividing the difference by the transmitted light power.

In the first experiment, a holographic grating with a grating spacing $\Lambda = 11.6$ μm was recorded in the completely poled crystal without any applied field. After the diffraction efficiency η reached its saturation value ($\eta = 11\%$), the recording beams were blocked, and a negative-voltage pulse with amplitude $V = -1$ kV and duration $t = 0.5$ s was applied to the crystal, which caused η to fall quickly. After the voltage pulse was removed, η recovered a portion of its initial value before the pulse. Then the crystal was illuminated with the non-Bragg-matched erasing beam, and η decreased further until it reached a steady-state value of $\eta \approx 0.06\%$. This fixed grating could not be erased by the erasing beam. Then the erasing beam was blocked, and a positive-voltage pulse, with amplitude $V = +2$ kV and duration of a

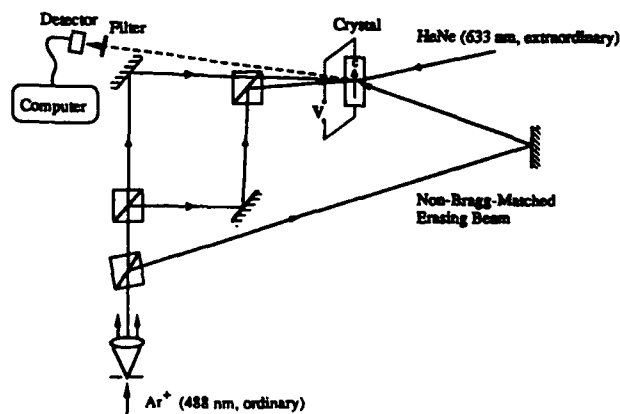


Fig. 1. Optical setup.

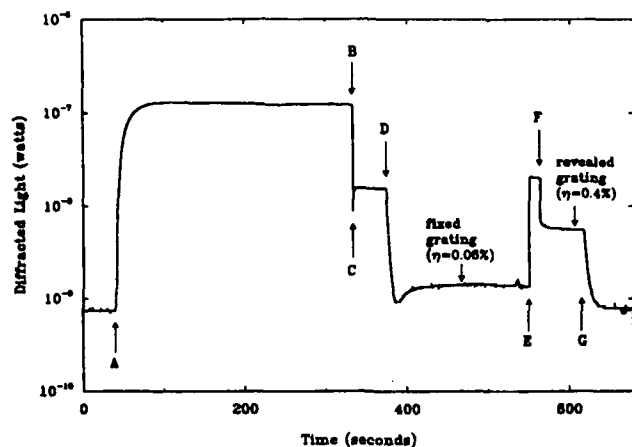


Fig. 2. Diffracted light as a function of time for fixing with a negative-voltage pulse ($\Lambda = 11.6 \mu\text{m}$). The transmitted light power in the absence of the grating is $1.1 \mu\text{W}$. A, Hologram recording begins. B, Negative pulse is applied. C, End of negative pulse. D, Optical erasure begins. E, Erasing beam is blocked and positive-voltage pulse is applied. F, End of positive pulse. G, Optical erasure begins.

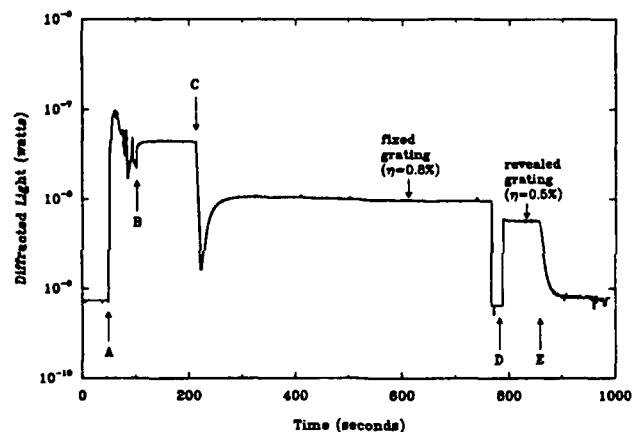


Fig. 3. Diffracted light as a function of time for fixing with a constant negative voltage during recording ($\Lambda = 11.6 \mu\text{m}$). The transmitted light power in the absence of the grating is $1.1 \mu\text{W}$. A, Hologram recording begins and negative voltage is applied. B, Negative voltage is removed and recording beams are blocked. C, Optical erasure begins. D, Positive-voltage pulse is applied (probe beam is blocked). E, Optical erasure begins.

few seconds, was applied to the crystal. During the positive-voltage pulse, $\eta = 1.8\%$, and after the pulse a grating with $\eta = 0.4\%$ was revealed. This revealed grating can be optically erased. The experimental results of recording, fixing, revealing, and erasing are shown in Fig. 2, where the diffracted signal is plotted as a function of time during the different stages of the experiment.

Comparing the results in Fig. 2 with Ref. 5, we see that we were able to achieve electrical fixing, but the fixed grating obtained in our experiment is much weaker than that in Ref. 5. Another important difference is our observation of a revealed grating on application of a strong positive voltage across the crystal at relatively large grating spacings.

We have found that in general the strengths of the fixed grating and the revealed grating can be greatly enhanced by applying a constant negative voltage during recording. With an applied voltage of $V = -500 \text{ V}$, we recorded a grating with $\Lambda = 11.6 \mu\text{m}$, using an exposure time of 50 s. Then the recording beams were blocked, the applied voltage was removed, and the grating was allowed to settle down to a steady level. On illumination of the crystal with the erasing beam, η decreased first and then rose back to a steady state, indicating a fixed grating of $\eta = 0.8\%$. Finally, a positive-voltage pulse, the same as the one used in the previous experiment, was applied, which revealed a grating of $\eta = 0.5\%$. This experimental result is shown in Fig. 3.

The experiment described above was repeated for several different grating spacings, and the results are summarized in Fig. 4. Under our experimental conditions, the maximum diffraction efficiency of the fixed grating is found to be 0.8% at $\Lambda = 11.6 \mu\text{m}$. The revealed grating is observed only for relatively large Λ , and its strength increases drastically with the increase in Λ , achieving approximately 17% diffraction efficiency at $\Lambda = 29 \mu\text{m}$.

Finally, an image was recorded in the crystal as an image plane hologram, and Fig. 5(a) shows the reconstruction of the hologram. Figure 5(b) shows the reconstruction of the fixed hologram. The fixed hologram did not show any sign of degradation un-

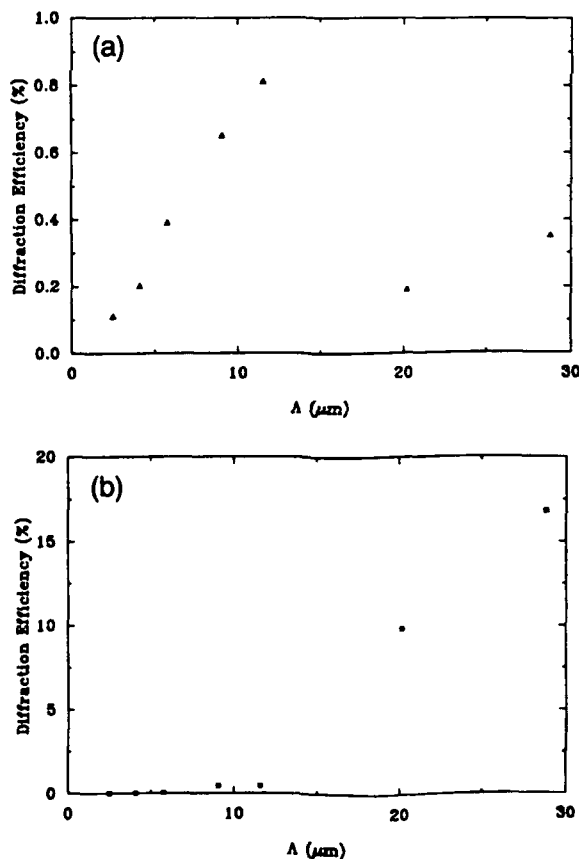


Fig. 4. Diffraction efficiency as a function of grating spacing for (a) the fixed grating and (b) the revealed grating.



Fig. 5. (a) Reconstruction of the recorded hologram and (b) reconstruction of the fixed hologram.

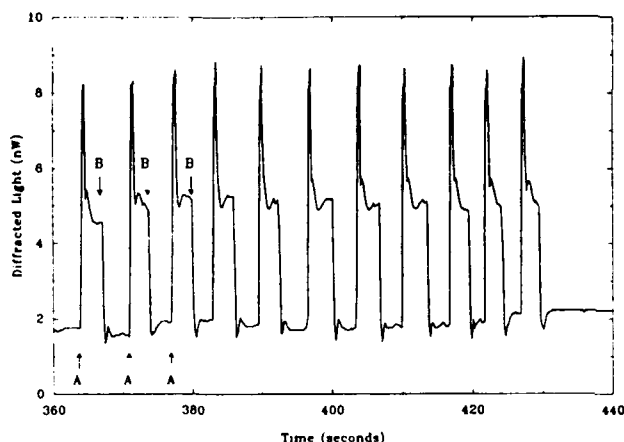


Fig. 6. Cyclic fixing and revealing of the stored hologram ($\Lambda = 20.2 \mu\text{m}$), with the erasing beam off during the entire process. A, Positive (revealing) pulse is applied, with $V = +1 \text{ kV}$. B, Negative (fixing) pulse is applied, with $V = -1 \text{ kV}$.

der illumination with the non-Bragg-matched erasing beam for 2.5 h.

The fixing-and-revealing process that we described was not observed when a positive rather than a negative fixing voltage was applied. If we assume that the mechanism responsible for fixing involves compensating ions, then we have no obvious explanation for the asymmetry regarding the polarity of the fixing voltage. Similarly, if the mechanism involved two types of photorefractive species,⁹ the effect would not be sensitive to the polarity of the fixing voltage. The fact that the fixed grating can be electrically erased nearly instantaneously (less than 0.1 s) in the dark (i.e., without redistribution of charge carriers among the trap sites) also indicates that the effect does not involve two types of trap site that compensate for each other. Therefore we believe that the mechanism responsible for this effect is the polarization grating formation suggested in Ref. 5.

Specifically, our observations can be explained as follows. With the aid of the negative external field, the electronic space-charge field established during the holographic recording causes a spatial modulation of the ferroelectric polarization. In the areas where the space-charge field is negative, the local polarization is modified (which corresponds to local

depoling or possible repoling in the opposite direction). This causes the decrease of both the mean linear electro-optic coefficient and the amplitude of the space-charge field modulation. As a result, the amplitude of the refractive-index modulation decreases on application of a negative voltage pulse, causing the drop in the monitored diffraction efficiency. Under the illumination of the erasing beam, the electronic grating is erased further, until a balance between the polarization grating and the electronic grating is reached. The fixed grating observed is attributed to the polarization grating for which the electronic grating partially compensates. Finally, a strong positive voltage applied to the crystal erases the polarization grating (i.e., the ferroelectric domains are realigned), revealing the compensating electronic grating, which of course can be erased optically. The enhancement of the diffraction efficiency of the revealed grating during the positive-voltage pulse (see Fig. 2) is attributed to the nonlinear electro-optic effect in SBN:75.¹⁰ We have developed a physical model that describes the above process, and the predicted dependence of the diffraction efficiencies on the grating spacing closely matches our experimental observations.¹¹

The above experiments suggest two modes of hologram fixing in SBN:75 crystals: the fixed polarization grating and the revealed electronic grating. Although the revealing process is destructive to the polarization grating, it is possible to recreate this grating by applying a negative-voltage pulse after the electronic grating is revealed. These revealing/fixing cycles were repeatedly performed (shown in Fig. 6), and the diffraction efficiency of the revealed grating (and thus the polarization grating) remained unchanged.

This research is supported by the Defense Advanced Research Projects Agency and the U.S. Air Force Office of Scientific Research. We thank Whye-Kei Lye for his help.

References

1. J. J. Amodei and D. L. Staebler, *Appl. Phys. Lett.* **18**, 540 (1971).
2. L. Arizmendi, *J. Appl. Phys.* **65**, 423 (1989).
3. G. Montemezzani and P. Günter, *J. Opt. Soc. Am. B* **7**, 2323 (1990).
4. D. Kirillov and J. Feinberg, *Opt. Lett.* **16**, 1520 (1991).
5. F. Micheron and G. Bismuth, *Appl. Phys. Lett.* **23**, 71 (1973).
6. F. Micheron and G. Bismuth, *Appl. Phys. Lett.* **20**, 79 (1972).
7. F. Micheron and J. Trotier, *Ferroelectrics* **8**, 441 (1974).
8. V. Leyva, A. Agranat, and A. Yariv, *Opt. Lett.* **16**, 554 (1991).
9. G. S. Trofimov and S. I. Stepanov, *Sov. Tech. Phys. Lett.* **10**, 282 (1984).
10. J. P. Wilde and L. Hesselink, *Opt. Lett.* **17**, 853 (1992).
11. S. Orlov, Y. Qiao, and D. Psaltis, "Dynamic compensation of fixed gratings in photorefractive media," submitted to *J. Opt. Soc. Am. B*.



Rockwell International
Science Center
SC71041.FR

APPENDIX 6.4

DYNAMIC ELECTRONIC COMPENSATION OF FIXED GRATINGS IN PHOTOREFRACTIVE MEDIA

Dynamic electronic compensation of fixed gratings in photorefractive media

Sergei Orlov and Demetri Psaltis
California Institute of Technology
Department of Electrical Engineering 116-81
Pasadena, California 91125

Ratnakar R. Neurgaonkar
Rockwell International Science Center
1049 Camino dos Rios
Thousand Oaks, California 91360

Abstract

We present a model describing the formation of a photorefractive grating in the presence of photorefractively- inactive space-charge modulation. The treatment is based on standard linearized Kukhtarev's equations. The model developed is applied to the interpretation of experimental results on electrical fixing in $\text{Sr}_{0.75}\text{Ba}_{0.25}\text{Nb}_2\text{O}_6$.

We present a model that describes the formation of a photorefractive grating in the presence of a fixed grating. In general, fixing methods demonstrated in different photorefractive crystals [1-7] create an optically unerasable charge or polarization distribution. The model predicts how the fixed grating affects the formation of the ordinary photorefractive grating and also leads to a spatially nonuniform mobile charge distribution even in the presence of a homogeneous illumination. There is good agreement between the predictions of the model and recent experimental results[7] on electrical fixing of holograms in $\text{Sr}_{0.75}\text{Ba}_{0.25}\text{Nb}_2\text{O}_6$.

The dynamic behavior of the photorefractive effect is described by the following set of nonlinear coupled equations[8]. We neglect the contribution of the photovoltaic effect and assume that only one type of carrier is involved:

$$\frac{\partial N_D^+}{\partial t} = (\alpha I_0 + \beta)(N_D - N_D^+) - \gamma_e n_e N_D^+ \quad (1)$$

$$j_e = e\mu n_e E + k_b T \mu \nabla n_e \quad (2)$$

$$\frac{\partial n_e}{\partial t} = \frac{\partial N_D^+}{\partial t} + \frac{1}{e} \nabla j_e \quad (3)$$

$$\nabla (P_s + \epsilon \epsilon_0 E) = e(N_D^+ - n_e - N_a + \rho_{fix}/e) \quad (4)$$

where N_D^+ - ionized donors concentration, n_e - free electron concentration, N_a - acceptor concentration, μ - carrier mobility, γ_e - recombination constant, P_s - spontaneous polarization, E - electric field. We consider a sinusoidal fixed charge distribution: $\rho_{fix} = \rho_{fix1} \exp(iKx)$ and spatially uniform light illumination I_0 . Following the usual linearization procedure and assuming that $\rho_{fix} \ll eN_a$, the quantities N_D^+ , n_e , E and j_e can be approximated by a sinusoidal form: $F(x) = F_0 + F_1 \exp(iKx)$. Assuming that P_s is uniform, the steady-state solution of the Eqs.(1-4

) for the space-charge field and the ionized donors density modulation is given by:

$$E_1 = \frac{\rho_{fix_1}}{iK\epsilon\epsilon_0} \cdot \frac{E_d - iE_0}{E_d + E_q - iE_0} \quad (5)$$

$$N_{D_1}^+ = -\frac{\rho_{fix_1}}{e} \cdot \frac{E_q}{E_d + E_q - iE_0} \quad (6)$$

where $E_d = Kk_bT/e$ -diffusion field, $E_q = N_E e / \epsilon\epsilon_0 K$ - limiting space-charge field, E_0 - external applied field. The time constant with which the field E_1 is formed is equal to the conventional grating formation time constant with the same average intensity and spatial frequency, formed in the absence of the fixed grating [9]. This is because the fixed grating acts as a nonhomogeneous term for the system of linearized Eqs. (1-4) replacing the sinusoidal intensity illumination; the coefficients of the set of linear equation remain unchanged, and hence the time constant is the same.

The total space-charge field (Eq. (5)) may be split into a sum of a field $\rho_{fix_1}/iK\epsilon\epsilon_0$ induced by fixed, nonphotorefractive charges and a compensating field E_1^{comp} formed by redistributed charge carriers described by $N_{D_1}^+$. Namely,

$$E_1^{comp} = \frac{eN_{D_1}^+}{iK\epsilon\epsilon_0} = -\frac{\rho_{fix_1}}{iK\epsilon\epsilon_0} \cdot \frac{E_q}{E_d + E_q - iE_0} \quad (7)$$

Note, that due to the finite dark conductivity, compensation of the fixed grating by dynamic electronic space-charge takes place even when no homogeneous illumination is present.

Our description so far assumed a fixed grating due to an ionic grating. Similar analysis may be applied to the case, where the fixed grating is produced by a spatial variation of the ferroelectric spontaneous polarization. A spatial variation of spontaneous polarization is formally equivalent to a fixed space-charge according to [10]: $\rho_{ind} = -\nabla P_s$. Then, assuming a sinusoidal modulation

of spontaneous polarization: $P_s = P_{s0} + P_{s1} \exp(iKx)$ the equation (4) takes the form:

$$\frac{\partial E}{\partial x} = \frac{e}{\epsilon \epsilon_0} \left(N_D^+ - n_e - N_a - \frac{1}{e} \frac{\partial P_s}{\partial x} \right) \quad (8)$$

or, in linearized form, for the case $E_0 = 0$:

$$iKE_1 = \frac{e}{\epsilon \epsilon_0} \left(N_{D1}^+ - n_{e1} - \frac{iK}{e} P_{s1} \right) \quad (9)$$

where ϵ - mean value of dc dielectric constant. The value of the total space-charge field E_1 and of the compensating electronic component E_1^{comp} are given by:

$$E_1 = -\frac{P_{s1}}{\epsilon \epsilon_0} \cdot \frac{1}{1 + E_q/E_d} = -\frac{P_{s1}}{\epsilon \epsilon_0} \cdot \frac{1}{1 + (\Lambda/\Lambda_e)^2} \quad (10)$$

$$E_1^{comp} = \frac{P_{s1}}{\epsilon \epsilon_0} \cdot \frac{E_q/E_d}{1 + E_q/E_d} = \frac{P_{s1}}{\epsilon \epsilon_0} \cdot \frac{(\Lambda/\Lambda_e)^2}{1 + (\Lambda/\Lambda_e)^2} \quad (11)$$

where $\Lambda = 2\pi/K$ - grating spacing and $\Lambda_e = 2\pi \sqrt{\frac{\epsilon \epsilon_0 k_B T}{e^2 N_E}}$ - Debye length.

The perturbation of the refractive index arises through the ordinary linear electrooptic effect due to the total space-charge field E_1 . Even though it is more correct to describe the refractive index variation in terms of polarization rather than electric field [11], both approaches lead to the same result and, in this sense, are equivalent. The modulation in spontaneous polarization also causes spatial variations of the linear EO coefficient and the dc dielectric constant. However, for the case of zero applied field considered here these terms do not contribute to the index of refraction variation.

In the case of fixing via ionic compensation the amplitude of the compensating electronic grating is difficult to measure independently, since the thermal erasure of the ionic grating also perturbs the electronic pattern. Electrical fixing which involves ferroelectric polarization, on the other hand, enables one to perform direct observations and measurements of the dynamic

compensating grating, since the polarization pattern can be erased simply by applying a strong positive electric field along the direction of spontaneous polarization of the PR crystal [6,7]. The latter process does not affect the compensating field E_1^{comp} , whose strength can then be determined by measuring the diffraction efficiency of the residual hologram.

We studied experimentally the process of fixing and compensation of phase holograms in photorefractive $\text{Sr}_{0.75}\text{Ba}_{0.25}\text{Nb}_2\text{O}_6$. Electrical fixing was achieved by applying a negative voltage pulse along the crystal c -axis after recording a space-charge grating with two input beams [7]. To avoid beam-coupling during recording and reconstruction, the ordinarily polarized beams were used and the holographic diffraction efficiency (HDE) was monitored by an extraordinarily polarized low-power He-Ne laser beam Bragg-matched to the initial hologram. A typical cycle of recording, fixation, optical and electrical erasure is shown on Fig.1. After the fixed hologram reaches steady state under illumination by a non-Bragg-matched erasing beam, a strong positive voltage pulse is applied erasing the polarization grating. The residual revealed hologram corresponds to the electronic compensating grating, which is measured by recording the power of light diffracted from it. Figure 2 shows the dependence of the steady-state values of the fixed HDE and the compensating revealed grating HDE with the grating spacing Λ . In agreement with the model proposed the amplitude of the electronic compensating grating (Eq. 11) dramatically increases with grating spacing.

Since in our experiments the effects associated with beam-coupling (i.e. longitudinal change of modulation index of hologram, self-depletion or self-enhancement) were carefully eliminated, the diffraction efficiency, in the limit of negligible absorption and small index variation, may be

expressed, as

$$\eta \simeq \left(\frac{\pi d |\Delta n_1|}{\lambda \cos \theta} \right)^2 \propto r_{eff}^2 E_1^2 \quad (12)$$

where d - crystal thickness, θ - Bragg angle inside the crystal, r_{eff} - effective linear EO coefficient, E_1 - internal space-charge field variation. Then, according to Eqs. (10) and (11), independent of the actual value of the polarization modulation, the ratio of HDEs of the fixed and compensating (or "revealed") gratings should obey the following relationship:

$$\ln \frac{\eta^{comp}}{\eta^{fix}} = 4 \ln \Lambda / \Lambda_c + 2 \ln r_{eff}^0 / r_{eff}^* \quad (13)$$

where r_{eff}^* is effective electrooptic coefficient of the partially depoled crystal after a negative depoling voltage is applied. The strong positive pulse that is applied to erase the polarization grating and to reveal the compensating grating also poles the crystal and, consequently, the EO coefficient takes its original value r_{eff}^0 . The experimental data shown on Fig.3 indicate a linear relationship between $\ln (\eta^{comp} / \eta^{fix})$ and $\ln \Lambda$ with slope $\simeq 4.2 \pm 0.2$ which is in a good agreement with the value 4, predicted by the theory (Eq. (13)). We should point out that since we don't know the dependence of P_{s1} with Λ the fact that the ratio plotted in Fig. 3 is independent of P_{s1} makes possible the comparison between theory and experiment. The ratio of the HDEs of the compensating and fixed gratings is the same for both an ionic or a polarization fixed grating. However, the fact that we could observe an optically erasable revealed compensation grating by electrically erasing the fixed grating, strongly favors the hypothesis that the fixing was due to polarization switching in the SBN fixing experiment [6,7]. The maximum modulation depth of the spontaneous polarization, corresponding to the maximum fixed grating HDE, was evaluated to be equal to $\Delta P_s \simeq 10^{-4} P_s$, where $P_s \simeq 8.1 \mu C / cm^2$ is the spontaneous polarization of the

completely poled $\text{Sr}_{0.75}\text{Ba}_{0.25}\text{Nb}_2\text{O}_6$ crystal at room temperature [6]. This small modulation depth is responsible for the weak fixed holograms.

In conclusion, we have presented a model for the formation of a grating in the presense of photorefractively inactive, fixed charge or polarization modulation. Application of this model to electrical fixing in $\text{Sr}_{0.75}\text{Ba}_{0.25}\text{Nb}_2\text{O}_6$ gives good agreement between experimental observations and theoretical predictions.

This work was supported by the Advanced Research Project Agency and the U.S. Air Force Office of Scientific Research. We thank Yong Qiao, Whye-Kei Lye, and Jiafu Luo for their help.

References

1. J.J. Amodei and D.L. Staebler, *Appl. Phys. Lett.* **18**, 540 (1971).
2. D. Kirillov and J. Feinberg, *Opt. Lett.* **16**, 1520 (1991).
3. G. Montemezzani and P. Gunter, *J. Opt. Soc. Am. B* **7**, 2323 (1990).
4. L. Arizmendi, *J. Appl. Phys.* **65**, 423 (1989).
5. V. Leyva, A. Agranat, and A. Yariv, *Opt. Lett.* **16**, 554 (1991).
6. F. Micheron and G. Bismuth, *Appl. Phys. Lett.* **23**, 71 (1973).
7. Y. Qiao, S. Orlov, D. Psaltis, and R. Neurgaonkar, *Opt. Lett.* **18**, (1993).
8. N. Kukhtarev, V. Markov, S. Odoulov, M. Soskin, and V. Vinetskii, *Ferroelectrics* **22**, 949 (1979).
9. G.C. Valley and J.F. Lam, in *Photorefractive Materials and Their Applications I*, P. Gunter and J.P. Huignard, eds. (Springer-Verlag, 1988), Chap. 3.
10. L.D. Landau and E.M. Lifshitz, *Electrodynamics of Continuous Media*, (Addison-Wesley, Reading, Mass., 1960), Chap. 2
11. W.D. Johnston, Jr., *J. Appl. Phys.* **41**, 3279 (1970).

Figure Captions

1. Figure 1: Diffracted signal as a function of time during the fixing experiment. Fixing pulse amplitude is -1650 V/cm and its duration 0.5sec . Total intensity of recording beams is 4mW/cm^2 , $\lambda = 488\text{nm}$, intensities ratio $m \approx 1$. The transmitted probe light power without the grating is $2.3\mu\text{W}$. A: recording begins. B: writing beams are blocked and a negative voltage pulse is applied. C: optical erasure with a non-Bragg-matched beam ($I = 8\text{mW/cm}^2$) begins. D: the transient dip due to 180° phase shift between the polarization and the electronic gratings. E: peak in HDE of the fixed grating; slow decay of fixed grating begins. F: steady state of the fixed grating. G: positive voltage pulse ($E = 4.2\text{kV/cm}$, duration 2 seconds) is applied (erasing beam is blocked). H: revealed compensating grating. I: optical erasure.
2. Figure 2: Diffraction efficiencies of fixed (steady state) and electrically revealed compensating gratings as a function of Λ . The same experimental parameters were used as in Fig.1.
3. Figure 3: Log-Log plot of the ratio of HDE's of the revealed compensating grating and the fixed grating vs. grating spacing. Points obtained for $\Lambda < 5.5\mu\text{m}$ were not included since the diffracted signal off the revealed hologram is less than the noise level. The linear fit has the slope 4.2 ± 0.2 which is in good agreement with the theoretically predicted value 4.0.

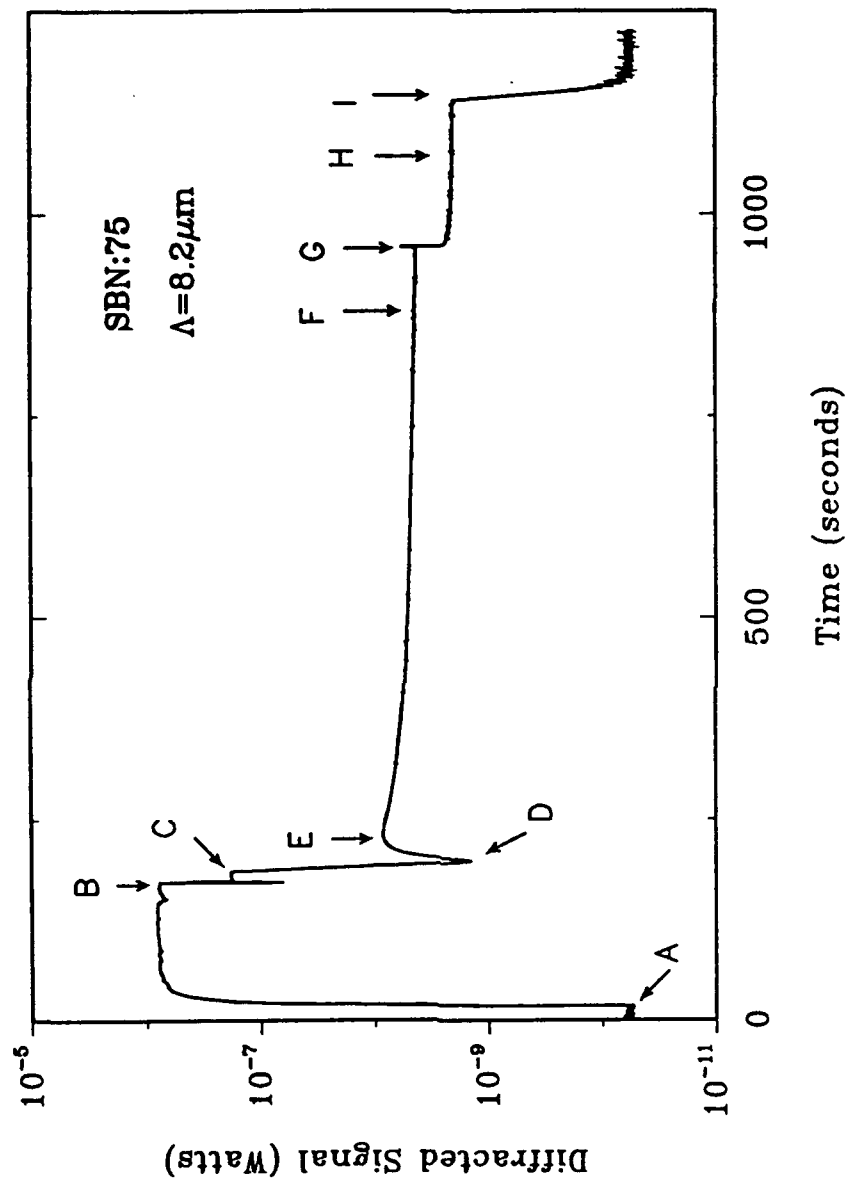


Figure 1

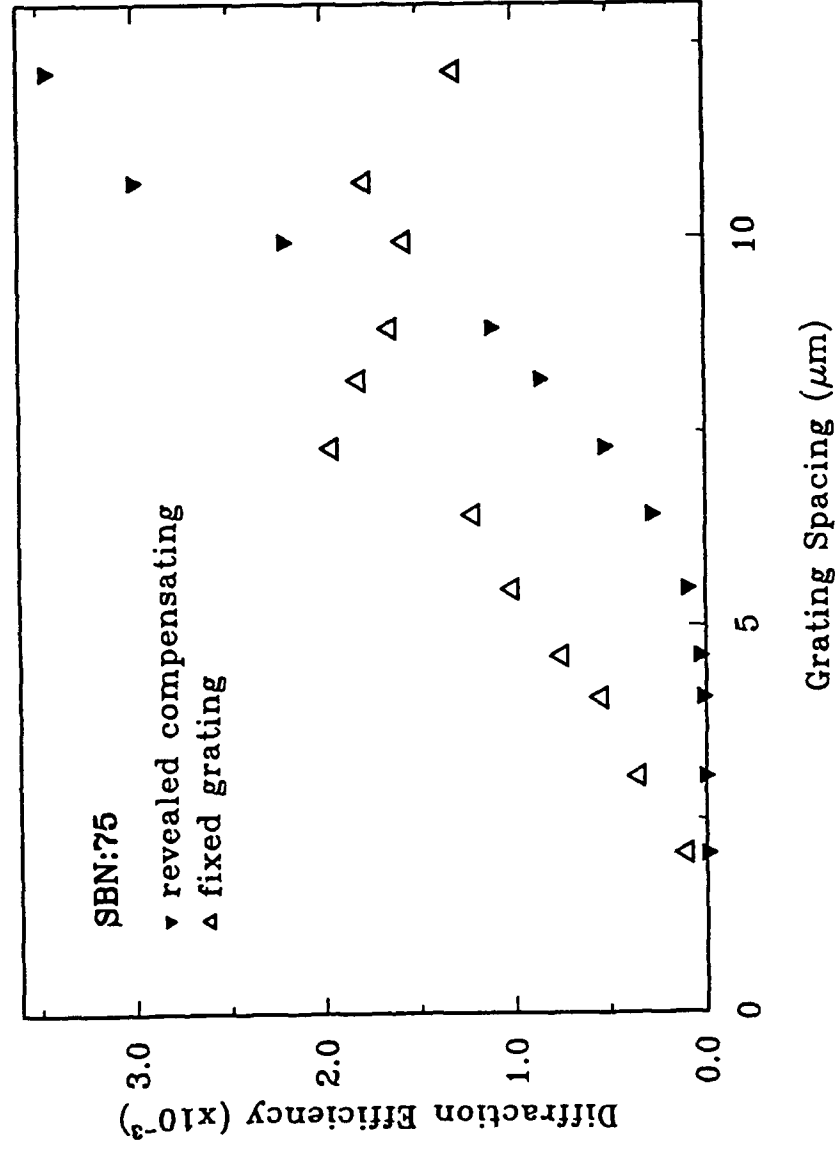


Figure 2

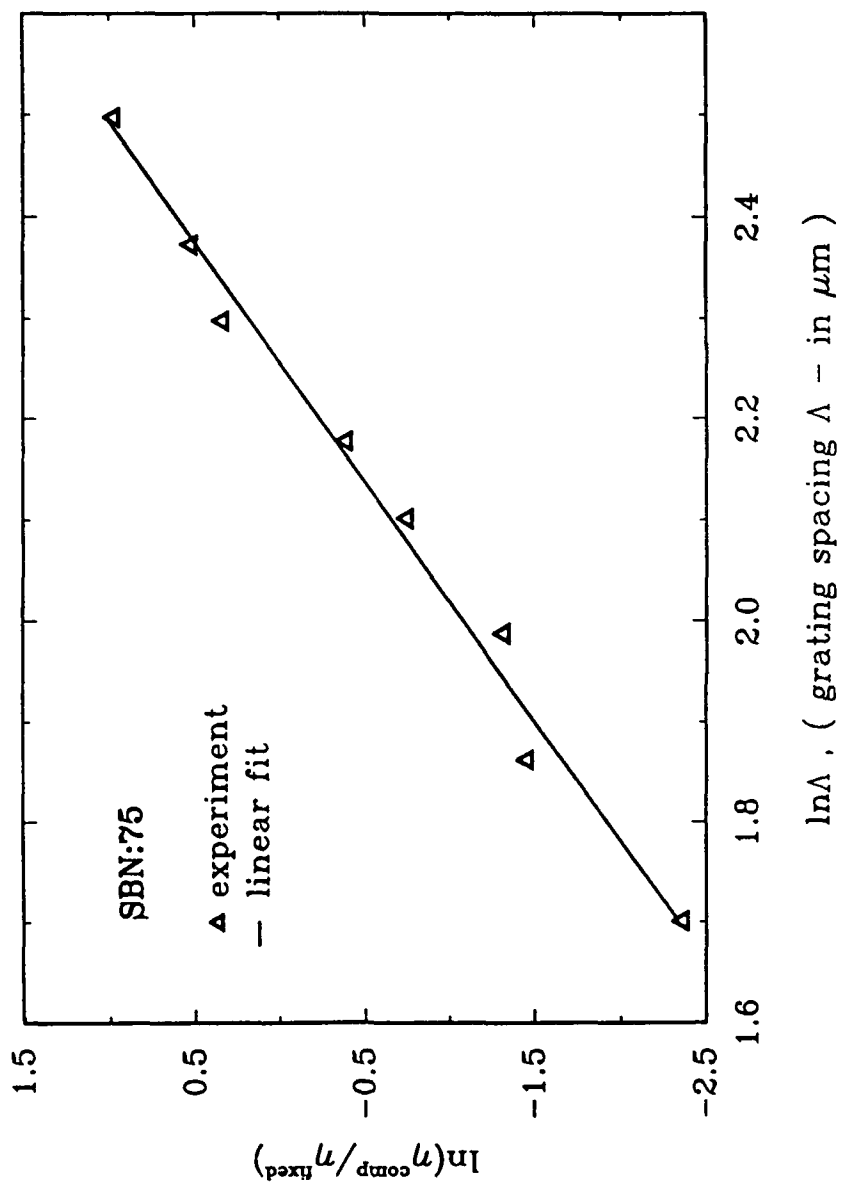


Figure 3



Rockwell International

Science Center

SC71041.FR

APPENDIX 6.5

ELECTRIC-FIELD MULTIPLEXING/DEMULTIPLEXING OF VOLUME HOLOGRAMS IN PHOTOREFRACTIVE MEDIA.

Electric-field multiplexing/demultiplexing of volume holograms in photorefractive media

Anthony Kewitsch, Mordechai Segev, and Amnon Yariv

Department of Applied Physics, California Institute of Technology, MS 128-95, Pasadena, California 91125

Ratnakar R. Neurgaonkar

Rockwell International Science Center, Thousand Oaks, California 91360

Received October 23, 1992

We propose a new method of volume hologram multiplexing/demultiplexing in noncentrosymmetric media. Volume holograms may be multiplexed by tuning the material parameters of the recording medium (such as refractive index or lattice parameters) while keeping the external parameters (wavelength and angles) fixed. For example, an external dc electric field alters the index of refraction through the electro-optic effect, effectively changing the recording and reconstruction wavelengths in the storage medium. Then the storage of holograms at different fields, hence different indices of refraction, is closely related to wavelength multiplexing. We demonstrate this concept in a preliminary experiment by electrically multiplexing two volume holograms in a strontium barium niobate crystal.

Holographic data-storage systems typically use angular,^{1,2} wavelength,³ or phase-coded^{4,5} multiplexing. Of these, the first two techniques exploit the dependence of the Bragg condition on the angle and wavelength of the writing beams:

$$\mathbf{K}_g = \mathbf{k}_1 - \mathbf{k}_2, \quad (1)$$

where $K_g = 2\pi/\Lambda_g$ is the magnitude of the grating vector, $k_1 = k_2 = 2\pi n/\lambda$ are the magnitudes of the reference and signal-beam wave vectors, respectively, Λ_g is the grating period, n is the index of refraction, and λ is the vacuum wavelength. However, the index of refraction is an additional degree of freedom in the Bragg condition that can be controlled by an external electric field.⁶ In this Letter we establish a relation between electric-field and wavelength multiplexing and present the results of a preliminary experiment that demonstrates the concept of field multiplexing.

We first derive a simple relation that illustrates the formal equivalence between wavelength and electric-field multiplexing under special conditions. This treatment is restricted to the case of counterpropagating signal and reference beams, both normally incident upon the crystal. In this case, the Bragg condition [Eq. (1)] becomes $\Lambda_g = \lambda/2n$, and the Bragg selectivity is maximal. Let us apply a field E to the crystal. Then, differentiating the Bragg condition at constant temperature T and mechanical stress σ , we obtain a relation for the change $\Delta\lambda$ required to maintain Bragg matching under field-induced changes $\Delta n(E)$ and $\Delta\Lambda_g(E)$:

$$\frac{\Delta\lambda}{\lambda} = \frac{\Delta n(E, \lambda)}{n} + \frac{\Delta\Lambda_g(E)}{\Lambda_g}. \quad (2)$$

Because the index of refraction in the crystal depends on the electric field and the wavelength,

$$\Delta n(E, \lambda) = \Delta n(E) + \frac{dn(\lambda)}{d\lambda} \Delta\lambda. \quad (3)$$

Substituting Eq. (3) into Eq. (2), we obtain a general relationship for the change in wavelength equivalent to a field-induced change of the index of refraction and grating period:

$$\frac{\Delta\lambda}{\lambda} = \frac{1}{(1 - \lambda/n \, dn/d\lambda)} \left[\frac{\Delta n(E)}{n} + \frac{\Delta\Lambda_g(E)}{\Lambda_g} \right]. \quad (4)$$

In a noncentrosymmetric crystal, the field induces an index change that is due to a combination of the electro-optic, elasto-optic, and piezoelectric effects⁷ and may rotate the principal axes by a field-dependent angle. We consider a simple yet common case, in which the optical and dc fields are parallel to the field-induced principal axes, and these axes do not rotate. Then the change in index along a principal axis is

$$\Delta n(E_k) = -\frac{n_o^3}{2} (r_{lk} E_k + p_{lm} d_{km} E_k), \quad (5)$$

where r_{lk} , p_{lm} , and d_{km} are the electro-optic, elasto-optic, and piezoelectric tensors, respectively, and $l = (ij)$ and $m = (np)$ in contracted notation. The field also induces a strain in the crystal, given by the second term on the right-hand side in Eq. (2):

$$\frac{\Delta\Lambda_g}{\Lambda_g} = d_{km} E_k. \quad (6)$$

Therefore this multiplexing technique is based on varying the material parameters such as the index of refraction and the lattice parameters. These parameters are also dependent on the temperature T

and mechanical stress σ , and a relation analogous to Eq. (4) is obtained on replacing E with T or σ for the cases of temperature or stress multiplexing. For the case of constant E and σ ,

$$\frac{\Delta\lambda}{\lambda} = \frac{1}{(1 - \lambda/n \, dn/d\lambda)} \left[\frac{\Delta n(T)}{n} + \frac{\Delta\Lambda_g(T)}{\Lambda_g} \right], \quad (7)$$

whereas for constant T and E ,

$$\frac{\Delta\lambda}{\lambda} = \frac{1}{(1 - \lambda/n \, dn/d\lambda)} \left[\frac{\Delta n(\sigma)}{n} + \frac{\Delta\Lambda_g(\sigma)}{\Lambda_g} \right]. \quad (8)$$

To simplify the analysis of electric-field multiplexing described by Eq. (4), we neglect the index dispersion $dn/d\lambda$ relative to n/λ [for strontium barium niobate (SBN:75), $\lambda/n \, dn/d\lambda \approx 0.2$, an error of 20%].⁸ The second term on the right-hand side of Eq. (4), the strain term, is in general of the order of $\Delta n/n$. Define a scale factor ξ_E according to

$$\frac{\Delta n(E)}{n} + \frac{\Delta\Lambda_g(E)}{\Lambda_g} \equiv \xi_E \frac{\Delta n(E)}{n}, \quad (9)$$

where ξ_E is assumed to be a slowly varying function of field E and typically $0 \leq |\xi_E| \leq 10$,⁹ depending on the sign and magnitudes of the linear electro-optic and piezoelectric coefficients. We define analogous scale factors for the temperature dependence

$$\frac{\Delta n(T)}{n} + \frac{\Delta\Lambda_g(T)}{\Lambda_g} \equiv \xi_T \frac{\Delta n(T)}{n}, \quad (10)$$

where $\Delta\Lambda_g = \alpha\Delta T$ (α is the thermal expansion coefficient), and for the stress dependence,

$$\frac{\Delta n(\sigma)}{n} + \frac{\Delta\Lambda_g(\sigma)}{\Lambda_g} \equiv \xi_\sigma \frac{\Delta n(\sigma)}{n}, \quad (11)$$

where the first term on the left-hand side is a piezooptical contribution and the second term is the strain. Then the index selectivity or index half-power bandwidth, defined as $|\Delta n|_{\text{FWHM}}$, for constant T and σ , is related to the spectral half-power bandwidth of a Bragg peak¹⁰ by Eqs. (4) and (9),

$$\frac{|\Delta n|_{\text{FWHM}}}{n} \approx \frac{1}{\xi_E} \frac{|\Delta\lambda|_{\text{FWHM}}}{\lambda} \approx \frac{1}{\xi_E} \frac{\Lambda_g}{L}, \quad (12)$$

where L is the thickness of the crystal. This expression relates the Bragg selectivity for field multiplexing to the familiar result for wavelength multiplexing. Because the grating period for two plane waves in this configuration is $\Lambda_g = \lambda/2n$, the minimum index change $\Delta n_{\text{min}} = 2|\Delta n|_{\text{FWHM}}$ between adjacent holograms written at the same wavelength is

$$\Delta n_{\text{min}} \approx \frac{\lambda}{\xi_E L}, \quad (13)$$

where the temperature and stress are assumed to be stabilized to within

$$\Delta T \ll \frac{\xi_E}{\xi_T} \Delta n_{\text{min}} \left(\frac{dn}{dT} \right)^{-1}, \quad (14)$$

$$\Delta \sigma \ll \frac{\xi_E}{\xi_\sigma} \Delta n_{\text{min}} \left(\frac{dn}{d\sigma} \right)^{-1}. \quad (15)$$

Therefore the number of holograms N_{holo} that can be multiplexed electrically is

$$N_{\text{holo}} = \frac{\Delta n_{\text{max}}}{\Delta n_{\text{min}}} \approx \frac{\xi_E L}{\lambda} \frac{dn}{dE} \Delta E_{\text{max}}. \quad (16)$$

To maximize N_{holo} , the crystal must satisfy two primary requirements. The material must have at least one large electro-optic coefficient that induces a significant index change for an electric field along (1) \mathbf{K}_g for beam coupling and (2) \hat{e}_1, \hat{e}_2 (the polarization vectors of the reference and signal) for electrically biasing the index of refraction. In addition, there are three conditions of secondary importance; it is desirable that the field does not rotate (3) the polarization or (4) the principal axes, and (5) the material should have a large piezoelectric tensor component d_{km} of the proper sign such that ξ_E is maximized. Failure to satisfy conditions (3) and (4) will reduce the beam coupling, because the polarization of the two beams will no longer remain parallel and in the desired direction of condition (2) as they propagate through the crystal.

The optimum geometry for electric-field multiplexing is achieved with counterpropagating signal and reference beams normally incident upon the crystal. This configuration has two primary advantages. First, the counterpropagating configuration exhibits inherently low cross talk and high wavelength selectivity.³ Second, it eliminates the detrimental Snell's law dependence of the angles in the crystal on the index of the crystal. In fact, for the transmission geometry with equal angles of incidence, the index dependence of the Bragg condition disappears:

$$2\Lambda_g n_{\text{crystal}} \sin \theta_{\text{crystal}} = 2\Lambda_g \sin \theta_{\text{air}} = \lambda. \quad (17)$$

Note, however, that the Bragg condition retains its field dependence $\Lambda_g(E)$ even in this case. In the optimal counterpropagating normally incident geometry discussed above, electric-field multiplexing is closely related to wavelength multiplexing (except that the photorefractive beam coupling and phase are now field dependent,¹¹ and the field induces a strain).

In the optimal reflection-grating geometry, we can estimate N_{holo} from relation (16). For typical parameters ($\lambda_0 = 0.5 \mu\text{m}$, $L = 1 \text{ cm}$, extraordinarily polarized signal and reference beams) and estimating $\xi_E \approx \xi_T \approx 1.25$, we calculate from relation (13) that $\Delta n_{\text{min}} = 4 \times 10^{-5}$. This implies from relation (14) that, for a material such as SBN:75 with $dn/dT = 2.5 \times 10^{-4}$,⁹ the temperature must be stable to within $T \ll 0.16 \text{ K}$ at 300 K. Because r_{33} is the only significant electro-optic coefficient in SBN:75, the optimal geometry is a compromise to satisfy simultaneously both conditions (1) and (2) (Fig. 1). This configuration also satisfies conditions (3) and (4). The total index tuning range in the optimized configuration is $\sim \Delta n_{\text{max}} = 0.0025$, half of $\Delta n_{\text{max}} = 0.005$ (Ref. 12) for a material such as SBN:75. Then the number of holograms that may be electrically multiplexed about λ_0 in SBN:75 is calculated from relation (16) to be ~ 60 .

In order to demonstrate experimentally the concept of electric-field multiplexing, we have used

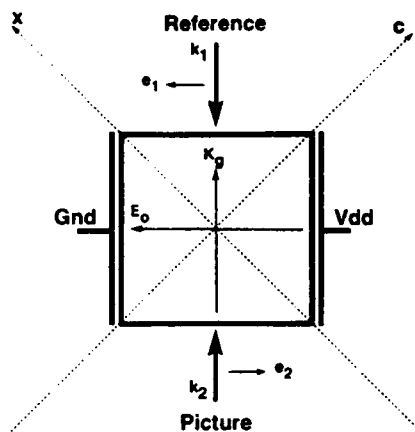


Fig. 1. Optimum configuration for electric-field multiplexing in SBN:75, with $r_{33} = 1340$ pm/V.

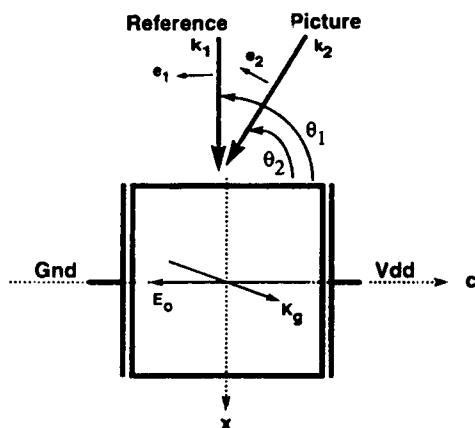


Fig. 2. Transmission configuration with external field applied opposite to the c axis.

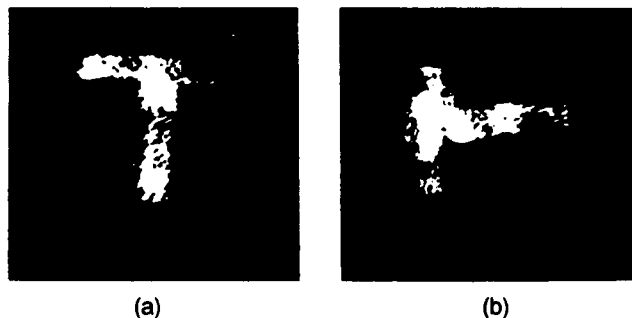


Fig. 3. Electric-field demultiplexing of two fixed holograms: (a) 0 V/cm, (b) 2000 V/cm.

$\text{Sr}_{0.75}\text{Ba}_{0.25}\text{Nb}_2\text{O}_6$ (SBN:75), with principal axes normal to the crystal faces. The orientation of the axes relative to the crystal faces (Fig. 2) prevents us from satisfying condition (1) in the counterpropagating configuration, because r_{33} is the only large electro-optic coefficient in SBN:75. Therefore, we performed a preliminary experiment in a transmission-grating configuration ($\theta_{1\text{air}} = 90^\circ$, $\theta_{2\text{air}} = 60^\circ$), which demonstrates the concept of electric-field multiplexing. A single fixed hologram at 0 V/cm may be switched

to the off-Bragg condition with a field increment as low as 500 V/cm and recovered when the field returns to 0 V/cm. In addition, we have individually fixed two holograms (angular bandwidth of images ≈ 4 mrad), one written with no external field [Fig. 3(a)] and another written with a field of 2000 V/cm [Fig. 3(b)]. (To the authors' knowledge, this is the first demonstration of selective fixing of individual holograms and will be reported elsewhere.¹³) The holograms are selectively addressed by reapplying the field at which they were written. As seen in the figures, the two holograms exhibit little cross talk (diffraction efficiency $\approx 1\%$). The holograms have also been demultiplexed by varying the angle of the reconstruction beam.

In conclusion, the addressing of individual holograms, which is usually performed by tuning the angle or wavelength of the reconstruction, is demonstrated by applying an electric field. This method can be used either independently or in combination with other addressing methods to fine tune the Bragg condition. For instance, electric-field multiplexing can be used in conjunction with wavelength multiplexing to tune continuously around discrete laser lines. Alternatively, field-multiplexed holograms can be angle or wavelength demultiplexed or vice versa.

This research is supported by the Army Research Office and the Air Force Office of Scientific Research. Anthony Kewitsch acknowledges the support of an Office of Naval Research graduate fellowship. We thank R. Hofmeister and S. Yagi for their assistance.

References

1. P. J. Van Heerden, *Appl. Opt.* **2**, 393 (1963).
2. F. H. Mok, M. C. Tackitt, and H. M. Stoll, *Opt. Lett.* **16**, 605 (1991).
3. G. A. Rakuljic, V. Leyva, and A. Yariv, *Opt. Lett.* **17**, 1471 (1992).
4. C. Denz, G. Pauliat, and G. Rosen, *Opt. Commun.* **85**, 171 (1991).
5. Y. Taketomi, J. E. Ford, H. Sasaki, J. Ma, Y. Fainman, and S. H. Lee, *Opt. Lett.* **16**, 1774 (1991).
6. S. Wu, A. Mayers, S. Rajan, and F. Yu, *Appl. Opt.* **29**, 1059 (1990).
7. J. F. Nye, *Physical Properties of Crystals, Their Representations by Tensors and Matrices* (Oxford U. Press, Oxford, UK, 1964).
8. E. L. Venturini, E. G. Spencer, P. V. Lenzo, and A. A. Ballman, *J. Appl. Phys.* **39**, 343 (1968).
9. E. Nakamura, ed., *Landolt-Börnstein, Ferroelectric Oxides*, New Series Vol. III/28a (Springer-Verlag, Berlin, 1990), Fig. 1272.
10. H. Kogelnik, *Bell Syst. Tech. J.* **48**, 2909 (1969).
11. M. Cronin-Golomb, B. Fischer, J. O. White, and A. Yariv, *IEEE J. Quantum Electron.* **QE-20**, 12 (1984).
12. J. B. Thaxter and M. Kestigian, *Appl. Opt.* **13**, 913 (1974).
13. A. Kewitsch, M. Segev, A. Yariv, and R. R. Neurgaonkar, "Selective page-addressable fixing of volume holograms in strontium barium niobate (SBN:75) crystals," submitted to *Opt. Lett.*



Rockwell International
Science Center
SC71041.FR

APPENDIX 6.6

BEAM COUPLING AND SPATIAL MODE CONVERSION IN PHOTOREFRACTIVE PLANAR WAVEGUIDES

**Beam Coupling and Spatial Mode Conversion
in Photorefractive Planar Waveguides**

Arthur Chiou, Pochi Yeh*, Claire Gu, and Ratnakar Neurgaonkar**

**Rockwell International Science Center
1049 Camino Dos Rios
Thousand Oaks, CA 91360
Tel: (805)373-4464, Fax: (805)373-4775
Internet: aechiou@scimail.remnet.rockwell.com**

Abstract

We discuss beam coupling and spatial mode conversion in photorefractive waveguides and their potential applications for efficient coupling of optical energy from a free-propagating mode to low-order guided modes. Experimental verification of the concept using a thin strontium barium niobate plate is reported.

*** University of California, Santa Barbara, CA**

**** Penn State University, University Park, PA**

Beam Coupling and Spatial Mode Conversion in Photorefractive Planar Waveguide

Arthur Chiou, Pochi Yeh*, Claire Gu**, and Ratnakar Neurgaonkar

Rockwell International Science Center, Thousand Oaks, CA 91360

* University of California, Santa Barbara, CA

** Penn State University, University Park, PA

Beam coupling in photorefractive bulk crystals has been studied intensively and demonstrated for many application concepts, including coherent image amplification, image processing and parallel logic operations.¹ In contrast, photorefractive beam coupling and spatial mode conversion in guided wave structures have attracted much less attention.²⁻⁶ The latter has potential application in facilitating the coupling of a free propagating laser beam to low-order guided modes in an appropriate waveguide structure.⁷ In this paper, we discuss this novel concept and present experimental demonstrations of beam coupling and spatial mode conversion in a thin plate of strontium barium niobate (SBN:75) crystal.

In a multimode waveguide or fiber, a higher order mode can be represented by a wave-vector K_2 propagating at an angle θ_2 (relative to the fiber axis) which is larger than the corresponding angle θ_1 associated with a lower order mode (Fig.1a). If the fiber is made of photorefractive material with c-axis parallel to the fiber axis, energy can be transferred from the higher order to the lower order modes via photorefractive beam coupling as the optical wave propagates towards the "+c" direction (Fig.1b). In principle, if the product of the coupling constant and the interaction length (ΓL) is sufficiently large (and assuming negligible loss), all the energy will eventually be transferred to the lowest order mode. In addition, the dynamic nature of the photorefractive grating can adaptively correct for certain changes in the input beam geometries such as the direction of beam injection and the beam profile. This process can therefore facilitate the coupling of a laser beam to a fiber or waveguide by not only improving the coupling efficiency but also reducing the sensitivity to misalignment.

In the following, we describe the experimental configurations and discuss the experimental results of beam coupling and mode conversion in a one-dimensional geometry using a photorefractive planar waveguide. The sample is a regular (xyz) cut SBN:75 plate (~9mmx10mmx1mm) with c-axis lying along the large a-face. Both a- and c- faces are optically polished.

For the study of multiple-beam coupling in discrete modes, four parallel beams originating from an argon laser (514.5nm) were focused and coupled into the plate from the c-face at different angle of incidence via a focusing lens L ($f = 63\text{mm}$) as illustrated in Fig.2a. The output of the signal beam (i.e., the one parallel to the c-axis) was monitored by a detector. When the beams are injected towards the "+c" direction, energy transfer from the other beams into the signal beam, and vice versa, was observed.

For the study of spatial mode conversion in a continuum of K-vectors, the four discrete beams were replaced by an expanded sheet of beams via appropriate cylindrical optics (Fig.2b). The fact that the mode conversion (from the higher order to the lower order, or vice versa) is due to photorefractive dynamic grating is verified by introducing a strong erasure beam (with polarization orthogonal to that of the signal beam) from the a-face.

As the erasure beam was turned on, the coupling decayed with the characteristic photorefractive time constant. The output signals with and without the presence of the erasure beam are shown in Fig.3. Quantitative characterization of the phenomena described above will be presented.

This work is supported by ARPA/AFOSR under contract No. F49620-92-0067.

References:

1. See, for example, P. Yeh, *Introduction to Photorefractive Nonlinear Optics* (Wiley, New York, 1993).
2. B. Fischer and M. Segev, "Photorefractive waveguides and nonlinear mode coupling effects," *Appl. Phys. Lett.* **54**, 684 (1989).
3. F. Ito and K. Kitayama, "Photorefractive crystal waveguide with periodically reversed c axis for enhanced two-wave mixing," *Appl. Phys. Lett.* **59**, 1932 (1991).
4. K. E. Youden, et al., "Photorefractive planar waveguides in BaTiO₃ fabricated by ion-beam implantation," *Opt. Lett.* **17**, 1509 (1992).
5. A. A. Kamshilin, et al., "Two-wave mixing in photorefractive Bi₁₂SiO₂₀ fibers," *Opt. Lett.* **18**, 690 (1993).
6. M. Zha, et al., "Two-wave mixing in photorefractive ion-implanted KNbO₃ planar waveguides at visible and near-infrared wavelengths," *Opt. Lett.* **18**, 577 (1993).
7. P. Yeh, "Reconfigurable optical interconnection," *Proc. SPIE* **1582**, 3 (1991).

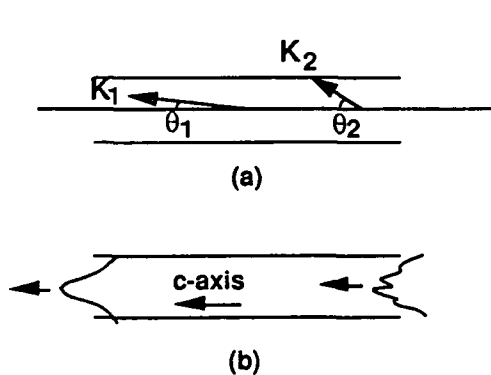


Fig.1 (a) Geometrical representation of wave-vectors associated with higher-order and lower-order modes in a multimode waveguide; (b) a conceptual illustration of spatial mode conversion in a photorefractive waveguide.

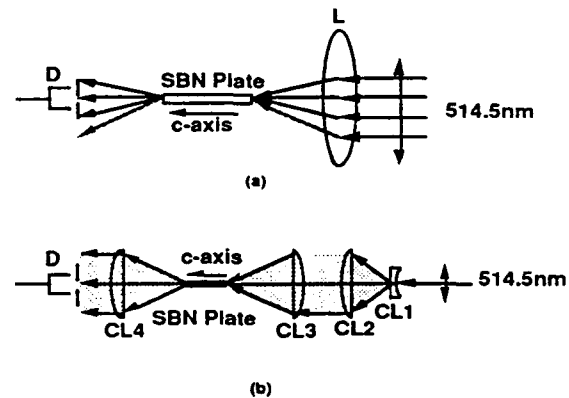


Fig.2 Experimental geometry for (a) beam coupling in discrete modes, (b) mode conversion in a continuum of K-vectors in a photorefractive planar waveguide.

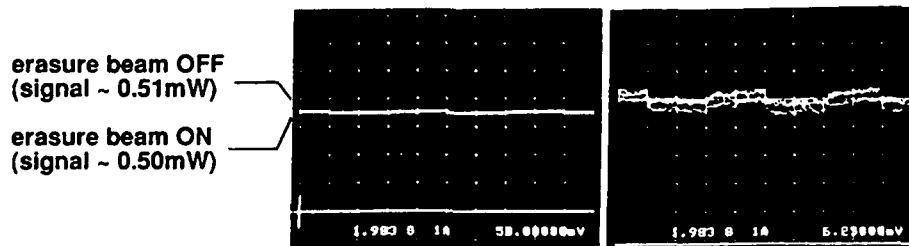
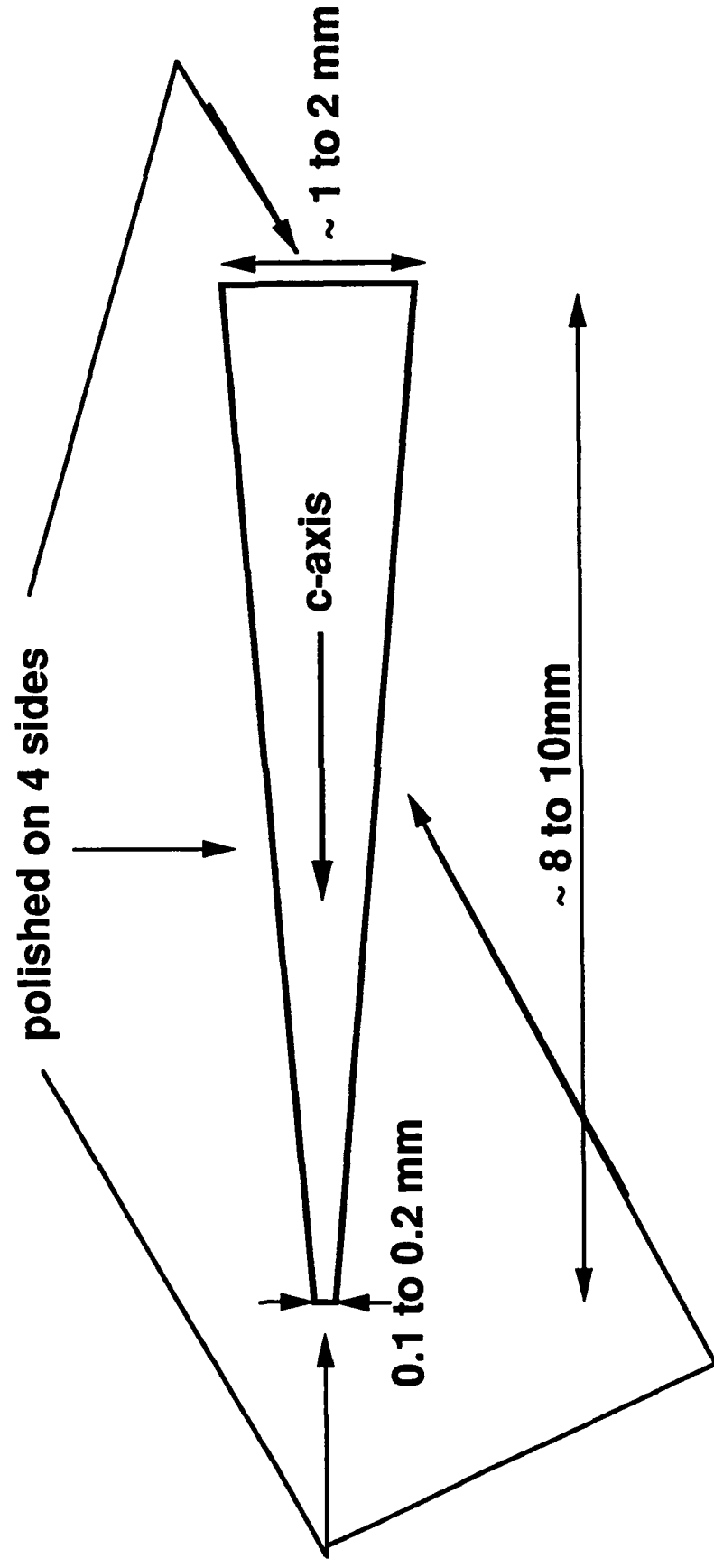


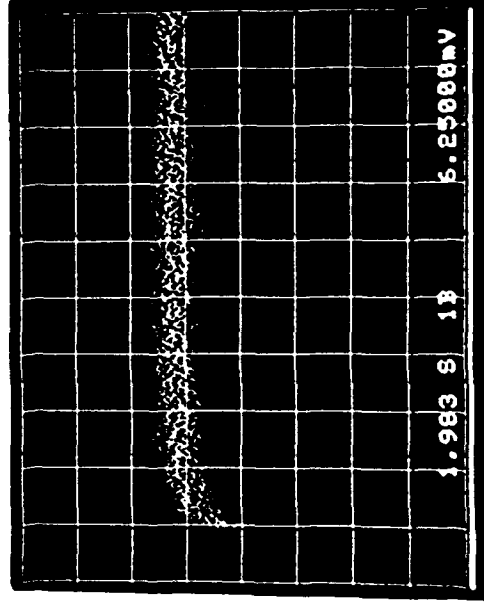
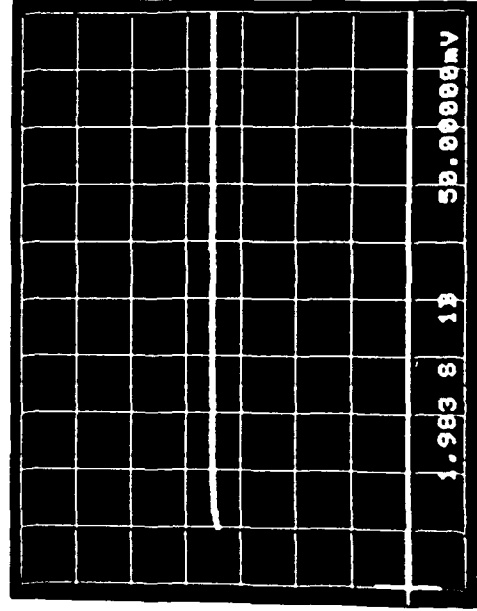
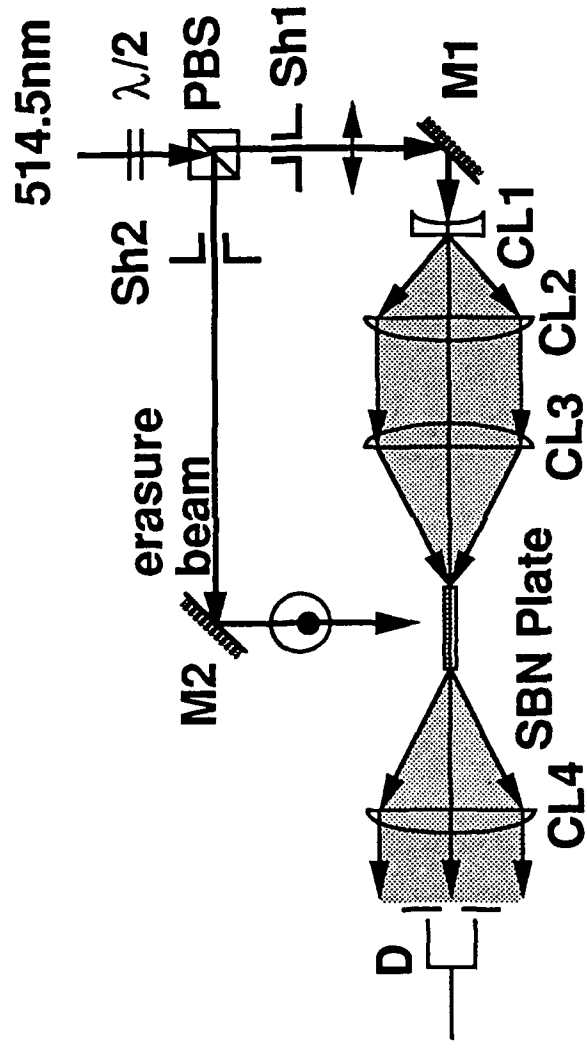
Fig. 3 Experimental results, corresponding to Fig. 2(b), showing the signal output with and without spatial mode conversion. The oscillograph on the right is a magnified (8x) version of the one on the left.

Photorefractive Wedge Sample (Top-View)

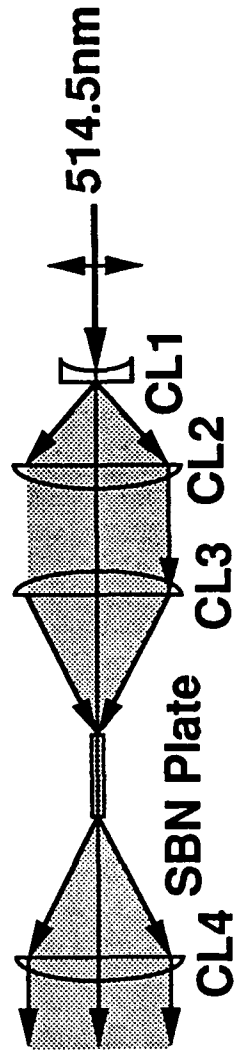
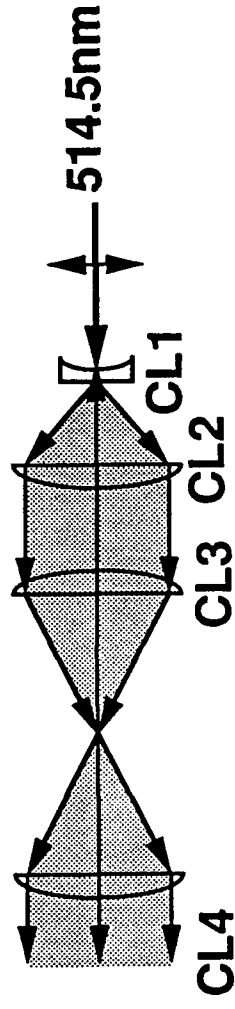
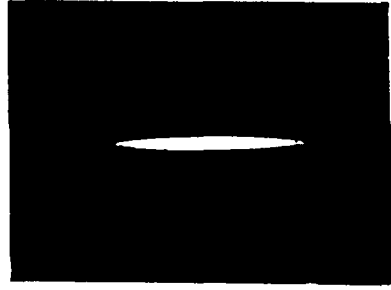


height of the wedge ~ 4 to 8 mm

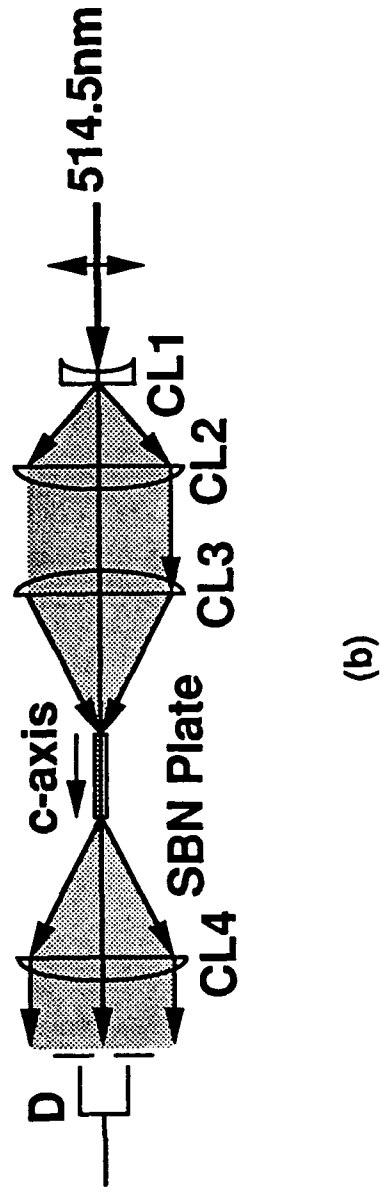
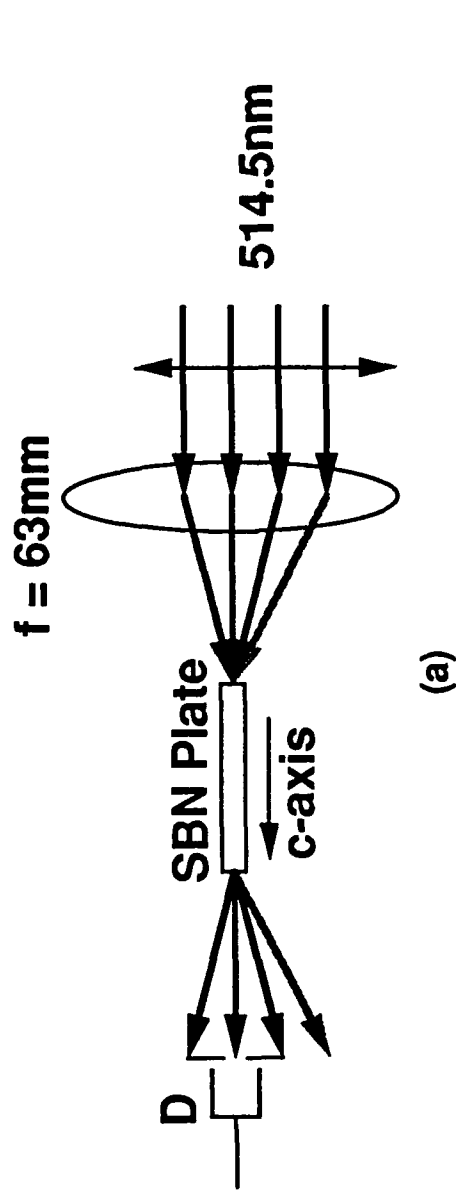
Spatial Mode Conversion in SBN Plate



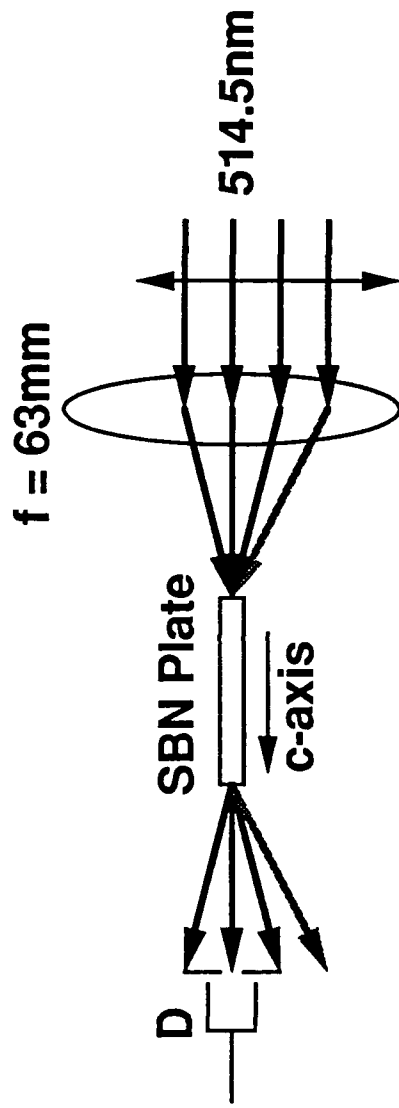
Spatial Mode Conversion in SBN Plate



Beam Coupling and Mode Conversion in an SBN Plate: Experimental Configurations



Beam Coupling in SBN Plate



with pump ON
(0.068mW)

signal only
(0.063mW)

